Research Square

Preprints are preliminary reports that have not undergone peer review.
They should not be considered conclusive, used to inform clinical practice,
or referenced by the media as validated information.

Autumn overcompensation following post-drought rewetting advances spring phenology

Lei Chen

lei.chen1029@gmail.com

Sichuan University https://orcid.org/0000-0001-7011-8782

Minghong Yu

Sichuan University

Yilei Jin

Key Laboratory of Bio-Resource and Eco-Environment of Ministry of Education, College of Life Sciences, Sichuan University, Chengdu 610041, China.

Jiajie Luo

Key Laboratory of Bio-Resource and Eco-Environment of Ministry of Education, College of Life Sciences, Sichuan University, Chengdu 610041, China.

Xinbo Wang

Key Laboratory of Bio-Resource and Eco-Environment of Ministry of Education, College of Life Sciences, Sichuan University, Chengdu 610041, China.

Hongshuang Gu

Sichuan University https://orcid.org/0000-0003-0609-7862

Haoyu Qiu

Sichuan University https://orcid.org/0000-0003-2401-7678

Anqi Yang

Key Laboratory of Bio-Resource and Eco-Environment of Ministry of Education, College of Life Sciences, Sichuan University, Chengdu 610041, China.

Ge Bai

Key Laboratory of Bio-Resource and Eco-Environment of Ministry of Education, College of Life Sciences, Sichuan University, Chengdu 610041, China.

Qin Yan

Sichuan University

Junkai Ma

Sichuan University

Josep Peñuelas

CREAF-CSIC https://orcid.org/0000-0002-7215-0150

Article

Keywords:

Posted Date: November 19th, 2026

DOI: https://doi.org/10.21203/rs.3.rs-11135353/v1

License: This work is licensed under a Creative Commons Attribution 4.0 International License.
Read Full License

Additional Declarations: There is **NO** Competing Interest.

Autumn overcompensation following post-drought rewetting advances spring phenology

Minghong Yu[1,2], Yilei Jin[1], Jiajie Luo[1], Xinbo Wang[1], Hongshuang Gu[1], Haoyu Qiu[1], Anqi Yang[1], Ge Bai[1], Qin Yan[1], Junkai Ma[1], Josep Peñuelas[3,4], Lei Chen[1,2*]

[1]Key Laboratory of Bio-Resource and Eco-Environment of Ministry of Education, Laboratory for Ex Situ Conservation and-Resource Utilization of Mountain Plants, College of Life Sciences, Sichuan University; Chengdu, China.

[2]Chengdu Botanical Garden; Chengdu, China

[3]Global Ecology Unit Center for Ecological Research and Forestry Applications (CREAF)- National Research Council (CSIC)- Universitat Autònoma de Barcelona (UAB), National Research Council (CSIC); Bellaterra, Barcelona, Spain.

[4]Center for Ecological Research and Forestry Applications (CREAF); Cerdanyola del Vallès, Barcelona, Spain.

*Correspondence: lei.chen1029@gmail.com

Abstract

Global warming and shifting precipitation regimes are increasing the frequency and intensity of post-drought rewetting events, with potentially persistent consequences for forest phenology. Spring phenology is commonly attributed to winter and spring temperatures, yet whether recovery from drought during the preceding growing season carries over to regulate subsequent spring phenology remains poorly understood. Here, combining ground observations of 535 tree species across 2,939 sites, three satellite-derived phenology products from 1981 to 2020 across the Northern Hemisphere and controlled post-drought rewetting experiments, we show that rewetting after drought delays autumn phenology and prolongs photosynthetic carbon acquisition, generating an overcompensatory recovery response that advances subsequent spring phenology. This cross-seasonal effect was associated with enhanced carbon gain and storage during post-drought recovery, suggesting that carbon acquired during autumn overcompensation carries over across seasons to promote earlier spring reactivation. CMIP6 projections indicate that this cross-seasonal legacy is likely to persist throughout the twenty-first century and strengthen under greater warming. Our findings identify autumn overcompensation as a previously underappreciated mechanism linking post-drought recovery to subsequent spring phenology, revealing how recovery from hydroclimatic extremes can reorganize seasonal carbon acquisition and phenological timing across years.

Main

Plant phenology governs the timing of recurrent biological events and underpins terrestrial ecosystem functioning[1,2]. In forests, the timing of budburst and leaf unfolding determines the onset of the growing season and strongly influences annual productivity[3–5]. Phenological transitions also regulate canopy exchanges of energy, water and carbon, with consequences for biogeochemical cycling, trophic interactions and ecosystem stability[1,6]. Climate warming has substantially altered tree phenology in recent decades, yet responses vary across species, regions and years, with both advances and delays increasingly reported[7–9]. Identifying the mechanisms underlying these divergent responses is therefore essential for predicting forest responses to climate change and their feedbacks to the terrestrial carbon cycle[10–12].

Spring phenology is primarily governed by the interacting effects of chilling during endodormancy and forcing during ecodormancy[13,14]. Warming can advance spring onset by accelerating forcing accumulation, yet delay budburst by reducing chilling accumulation and thereby increasing the subsequent forcing requirement[15]. Temperature, however, is not the sole determinant of spring reactivation. Trees must assimilate and store sufficient carbon before winter because they rely on nonstructural carbohydrate reserves to sustain metabolism during dormancy and support early-season growth[16]. This suggests that spring phenology reflects a thermal-metabolic trade-off, whereby accumulated carbon reserves modulate thermal requirements for spring development. Recent studies suggest that growing-season warming can enhance carbon assimilation and carbohydrate accumulation, promoting earlier growth in the following spring[17]. Climate change, however, is also increasing the occurrence of extreme events, including drought and frost, that disrupt carbon uptake and alter the reserves available for subsequent growth[18,19]. Despite substantial understanding of the thermal regulation of dormancy transitions, how climatic extremes alter growing-season carbon gain and thereby carry over to influence spring phenology remains poorly understood.

Drought is among the most pervasive of these extremes, suppressing tree growth and increasing mortality risk[20,21]. By reducing photosynthetic carbon assimilation and depleting nonstructural carbohydrate reserves, drought can constrain both immediate survival and subsequent growth[22–24]. Droughts are also increasingly terminated by intense rainfall, generating recurrent post-drought rewetting events rather than isolated periods of water limitation[25,26]. Although drought generally suppresses productivity, post-drought rewetting can stimulate compensatory growth and, in some cases, overcompensatory carbon uptake[27–29], such that cumulative carbon gain during recovery exceeds that under continuously wet conditions and restores carbohydrate reserves above baseline levels before dormancy. Yet the recovery phase has received less attention than the drought itself[30]. It therefore remains unclear whether post-drought rewetting induces overcompensatory recovery and, if so, how this response carries over to regulate spring phenology in the following year. Resolving this cross-seasonal linkage is essential for predicting forest productivity and stability under increasingly variable hydroclimatic conditions[31].

Here, we integrated long-term ground observations of 535 tree species across 2,939 sites, three satellite-derived phenology datasets spanning the Northern Hemisphere from 1981 to 2020, and a controlled post-drought rewetting experiment to test whether post-drought recovery generates overcompensatory carbon gain that carries over to

subsequent spring phenology. We examined autumn phenology and productivity together because they capture complementary dimensions of carbon acquisition during recovery. Autumn phenology determines the duration of the carbon-uptake period, whereas productivity reflects the amount of carbon gained within that window. Post-drought rewetting may therefore generate overcompensation by both extending the carbon-acquisition period and increasing carbon gain during recovery. Specifically, we first quantified the hemispheric-scale effects of post-drought rewetting on spring phenology in the following year, autumn phenology, and ecosystem productivity in the current year. We then used the controlled experiment to test whether enhanced photosynthetic carbon gain and nonstructural carbohydrate storage during recovery mediate subsequent spring reactivation. Finally, we used CMIP6 projections to assess how these cross-seasonal effects may shape future forest phenology and productivity under different emission scenarios. We hypothesized that post-drought rewetting delays autumn phenology and enhances productivity, together generating overcompensatory carbon gain that persists across seasons and advances spring phenology in the following year.

Results

Effects of post-drought rewetting on phenology and productivity

To examine how post-drought rewetting influences subsequent spring phenology, we integrated three long-term and large-scale ground-based monitoring networks in Europe, Russia, and China and compiled 144,424 records of 535 species from 2,939 sites across the Northern Hemisphere between 1981 and 2020 (Fig. 1a and Table S2). To extend spatial coverage and cross validate ground observations, we further extracted phenological metrics from three independent satellite products GOSIF-GPP, MODIS-NBAR, and GIMMS NDVI3g (Table S1). Spring and autumn phenological events, marking the start (SOS) and end (EOS) of the growing season in both ground observations and satellite products, were recorded or expressed as day of year (DOY) (Methods).

We defined post-drought rewetting (DRW) as an event in which the SPEI value first dropped below −1 and subsequently recovered above −1 during the growing season, and constant-wetting (CW) as the SPEI value consecutively above −1. To assess the effects of DRW on phenology, we compared spring phenology in the next year (SOS_{next}) and autumn phenology in the current year ($EOS_{current}$) at each site or pixel between CW and DRW (Methods). To further examine differences in phenology across regions and vegetation biomes, we classified study sites into warm and cold regions based on their long-term median mean annual temperature, and vegetation types were categorized as deciduous, evergreen, and mixed forests.

Across the three ground-based phenological observation datasets, we found that DRW fundamentally restructured the annual cycle, inducing a cross-seasonal growing season extension by advancing SOS_{next} (Fig. 1b, c) and delaying $EOS_{current}$ (Extended Data Fig. 1). Among all three datasets, SOS_{next} advanced 2.70 ± 0.07 days, 1.36 ± 0.46 days, and 4.79 ± 0.51 days in PEP725, RCNN, and CPON, respectively (Fig. 1b and Table S3). We further examined species-level variability in phenological responses to DRW and CW using the PEP725 network, as it provides the most extensive phenological records and the longest temporal coverage. Four representative European tree species, including

Aesculus hippocastanum L., *Betula pendula* Roth., *Fagus sylvatica* L., and *Quercus robur* L., were chosen for their broad geographical distribution across Europe. We found that SOS_{next} of all species was significantly advanced (Fig. 1c), while $EOS_{current}$ was significantly delayed except *Aesculus hippocastanum* L. (Extended Data Fig. 1b).

Remote-sensing datasets, including GOSIF-GPP, MODIS-NBAR, and GIMMS NDVI3g products, revealed consistent patterns with ground-based observations, with DRW generally advancing SOS_{next} (Fig. 2a and Extended Data Fig. 2a, d) and delaying $EOS_{current}$ (Fig. 3c and Extended Data Fig. 4a, d) compared to CW. We further examined the relationship between $EOS_{current}$ and SOS_{next} across all remote-sensing datasets using SMA regression and found that later autumn phenology was associated with earlier spring phenology in the following year (Extended Data Fig. 5). To investigate spatial variation in climate–phenology relationships, we examined phenological responses across thermal gradients and vegetation types (Methods). DRW effects were generally stronger across seasons in warm regions for both SOS_{next} and $EOS_{current}$ than in cold regions (Fig. 2b, 3d and Extended Data Fig. 2b, e, 4b, e). Phenological divergence between the DRW and CW treatments was markedly smaller in mixed forests than deciduous and evergreen forests (Fig. 2c, 3e and Extended Data Fig. 2c, f, 4c, f). To test the robustness of these results, linear mixed-effects models were further applied to test whether DRW effects on SOS_{next} and $EOS_{current}$ varied across thermal regions and vegetation types by pooling all pixel-level records. We consistently found that DRW effects were weaker in colder regions and mixed forests (Table S5–7).

To examine whether post-drought rewetting induces overcompensatory carbon uptake, we calculated pixel-level differences in gross primary productivity (ΔGPP) and net primary productivity (ΔNPP) between DRW and CW, and assessed relationships between forest productivity and phenology across three remote-sensing products (see Methods). Using GOSIF products, we observed that DRW events had a positive impact on photosynthetic productivity, with a greater proportion of pixels showing an increase (Fig. 3a–b). Correlation analyses with SMA regression revealed negative relationships between forest productivity and SOS_{next} under DRW for both GPP ($r = -0.67$, $P < 0.001$) and NPP ($r = -0.66$, $P < 0.001$), indicating that higher carbon accumulation was associated with earlier subsequent spring phenology (Fig. 4a–b). Besides, $EOS_{current}$ shifts were positively correlated with GPP ($r = 0.67$, $P < 0.001$) and NPP ($r = 0.66$, $P < 0.001$) under DRW, indicating that higher forest productivity was associated with later autumn phenology (Fig. 4c–d). Similar results have also been obtained in MODIS and GIMMS products (Extended Data Fig. 3, 6, 7). These findings suggested that post-drought rewetting induces overcompensatory carbon gain by delaying autumn phenology and thereby extending the period of photosynthetic carbon uptake.

Experimental evidence for post-drought overcompensation and phenological carry-over

To experimentally test the observed overcompensatory response and its carry-over effects on subsequent spring phenology, we conducted a controlled post-drought rewetting experiment using two-year-old seedlings of four representative native tree species spanning deciduous and evergreen functional types (Extended Data Fig. 9). We monitored both tree phenology and non-structural carbohydrate (NSC) dynamics to explore how DRW altered carbon assimilation and shaped subsequent phenology.

Consistent with the hemispheric-scale analysis, DRW significantly advanced SOS_{next} and delayed $EOS_{current}$ relative to CW, with both effects being more pronounced in evergreen than in deciduous species (Fig. 5a–b). We also observed a negative correlation between $EOS_{current}$ and SOS_{next} in the experiment (Extended Data Fig. 10). The NSC concentrations were significantly higher under DRW than under CW, with a greater increase in deciduous than in evergreen species (Fig. 5c). In deciduous species, both starch and soluble sugar concentrations increased significantly under DRW, whereas in evergreen species only starch concentrations were significantly higher under DRW than under CW (Extended Data Fig. 11). Total chlorophyll concentrations were also significantly higher under DRW than under CW across all tree species, indicating an overcompensatory recovery of photosynthetic capacity following post-drought rewetting (Fig. 5d).

Correlation analyses revealed a negative correlation between NSC and SOS_{next} ($r = -0.88$, $P < 0.05$) (Fig. 6a), and a positive correlation between $EOS_{current}$ and NSC ($r = 0.72$, $P < 0.05$) (Fig. 6c). However, component-specific analyses showed that starch concentrations were negatively correlated with SOS_{next} ($r = -0.97$, $P < 0.05$) and positively correlated with $EOS_{current}$ ($r = 0.86$, $P < 0.05$) (Fig. 6b, d), whereas soluble sugar concentrations showed no significant correlations with either phenophases (Extended Data Fig. 12). To further test the carbon-mediated hypothesis, we constructed a piecewise structural equation model (SEM) to explore the direct and indirect effects of DRW on NSC and phenology (Fig. 6e, and Table S10). We found that DRW directly delayed $EOS_{current}$, thereby contributing to the advancement of SOS_{next}, but its direct effects on NSC and SOS_{next} were non-significant. Additionally, the DRW-induced delay in $EOS_{current}$ significantly increased NSC concentrations, which in turn significantly advanced SOS_{next}, indicating that the effect is entirely mediated by the biological recovery. Effect decomposition analysis further showed that effect of NSC on SOS_{next} was stronger than $EOS_{current}$ (Fig. 6f and Table S11). These results provide experimental evidence that DRW induced overcompensatory carbon gain by delaying autumn phenology, enhancing photosynthetic capacity and increasing carbon storage, with these responses carrying over to advance spring phenology in the following year.

Future projections of post-drought overcompensation and its phenological consequences

To project the future impacts of DRW on productivity and phenology, we analyzed phenological, GPP, and NPP outputs from four CMIP6 models (NorESM2-MM, CAS-ESM2-0, CMCC-ESM2-SR5, and CMCC-ESM2) under four CO_2 emission scenarios (SSP1-2.6, SSP2-4.5, SSP3-7.0, and SSP5-8.5). Future DRW and CW conditions were identified for each pixel based on projected SPEI-3 values, following the same classification approach applied to historical data. $EOS_{current}$ and SOS_{next} were evaluated across four successive 20-year intervals (2021–2040, 2041–2060, 2061–2080, and 2081–2100), while changes in GPP (ΔGPP) and NPP (ΔNPP) between DRW and CW conditions were calculated for each pixel from 2021 to 2100 (Methods). Consistent with historical observations, DRW generally advanced SOS_{next} and delayed $EOS_{current}$ across all emission scenarios and projection periods (Fig. 7a–b, and Extended Data Fig. 13a–b), suggesting that the phenological effects of DRW may already be emerging and could persist throughout the 21st century under future climate scenarios. Additionally, under DRW conditions, mean annual ΔGPP and ΔNPP were predominantly positive across all emission scenarios, with the proportion of increases in GPP and NPP attributable to

DRW rising progressively from SSP1-2.6 to SSP5-8.5 and reaching a maximum under SSP5-8.5 (Fig. 7c–d, and Extended Data Fig. 13c–d).

Discussion

Integrating large-scale observations with controlled experiments, we found that rewetting delayed autumn phenology and prolonged the period of carbon acquisition, while simultaneously enhancing photosynthetic productivity during recovery. Together, these responses generated overcompensatory carbon gain, accompanied by greater nonstructural carbohydrate storage and earlier spring phenology in the following year. These findings show that post-drought recovery can extend beyond the restoration of pre-drought function, generating compensatory carbon gains that offset drought-induced losses and carry over across seasons to reshape phenological dynamics. Therefore, our results identify autumn overcompensation as a previously overlooked mechanism linking post-drought rewetting to subsequent spring phenology.

Autumn overcompensation carries over to subsequent spring phenology

We propose two possible hypotheses to explain the observed advance in spring phenology after post-drought rewetting. One possibility is that delayed autumn phenology alters dormancy progression, thereby shifting spring phenology in the following year. Because autumn phenology marks the transition into dormancy, later senescence could reduce the time available for dormancy development and potentially delay subsequent spring leaf-out[32]. However, our results do not support this interpretation. Although post-drought rewetting delayed autumn phenology, spring phenology advanced rather than delayed, and no positive relationship was detected between autumn and subsequent spring phenology. This suggests that delayed autumn phenology did not primarily influence spring timing through changes in dormancy progression[33,34].

Instead, our results support a carbon-driven mechanism whereby post-drought rewetting induces overcompensatory carbon assimilation and storage, which in turn advances spring phenology in the following year. Several lines of evidence support this interpretation. Trees rely on nonstructural carbohydrates accumulated before winter to survive dormancy and support early-season growth[16,35], indicating that spring phenology is shaped not only by dormancy regulation, but also by carbon conditions carried over from the previous growing season[36]. Greater carbohydrate reserves may modify the carbon-forcing trade-off in spring phenology, partly relax dependence on thermal forcing by supplying the energy required and providing substrates required for early spring development[37,38]. Consistent with this view, recent studies have shown that warming can enhance photosynthetic carbon assimilation and carbohydrate storage, thereby advancing leaf unfolding in the following year[17]. By contrast, drought may delay green-up and leaf-out in the subsequent spring, probably because it reduces carbon assimilation during the previous growing season[39]. Here, we found that both GPP and NPP increased after drought followed by rewetting, indicating that post-drought recovery involved not merely compensation for drought-induced losses, but an overcompensatory increase in productivity[27]. High early-season productivity can trigger earlier senescence via sink saturation[40], but our results demonstrate that late-season compensatory carbon gain following drought release sustains metabolic activity, delaying autumn phenology and overriding the sink-limitation signal. This post-drought

overcompensation likely increased NSC storage, providing additional carbon reserves to support spring growth and thereby advancing spring phenology in the following year.

This interpretation was further supported by the observed relationships among EOS, NSC, and subsequent SOS. Rewetting can restore leaf water status and stomatal conductance, enabling rapid recovery of photosynthesis[41]. Where drought does not cause persistent hydraulic or photosynthetic impairment, trees can rapidly resume carbon assimilation after rehydration[42]. Moreover, drought-induced increases in abscisic acid rapidly decline following rewetting, whereas cytokinin levels rise, potentially counteracting stress-induced senescence signals[43]. This hormonal reset may further delay autumn senescence and prolong late-season canopy activity, thereby extending the period available for photosynthetic carbon assimilation[44,45]. Consistent with this mechanism, our controlled experiment showed that later EOS was associated with higher NSC storage, and that greater NSC reserves were linked to earlier SOS in the following year. These relationships provide experimental evidence that post-drought rewetting can delay autumn phenology and enhance carbon accumulation, thereby advancing subsequent spring phenology. Therefore, shifts in autumn phenology induced by post-drought rewetting may function less as a direct regulator of subsequent spring timing than as a carbon-acquisition strategy that increases reserves available for future development. Furthermore, starch, rather than soluble sugars, is more tightly coupled to tree phenology, consistent with its role as a persistent carbon reserve linking carbon acquisition across seasons to subsequent budburst, whereas soluble sugars largely reflect short-term metabolic and osmotic dynamics[35].

These findings have broader implications for predicting forest responses to increasingly variable hydroclimatic regimes. Although drought is widely recognized as a major constraint on tree growth and ecosystem productivity, its consequences depend critically on the subsequent recovery phase[46]. When drought is followed by substantial rewetting, recovery may involve overcompensatory carbon gain that generates cross-seasonal phenological legacies. Thus, the effects of drought on spring phenology cannot be inferred from drought stress alone, but must also account for the timing and magnitude of post-drought rewetting. More broadly, our findings reveal that overcompensatory carbon acquired during recovery can carry across seasons, coupling climate extremes with ecosystem recovery and subsequent phenological change.

Variations among tree species, regions, and vegetation types

We consistently observed advanced spring phenology and delayed autumn phenology following post-drought rewetting across tree species, regions and vegetation types, yet the magnitude of these shifts varied, indicating strong context dependence. Across thermal gradients, responses were more pronounced in warm than in cold regions. The weaker response in cold regions suggests that the recovery window is thermally constrained, with insufficient growing degree-days limiting the capacity of trees to translate post-drought rewetting into substantial overcompensatory carbon gain before winter dormancy[31]. Although warmer environments are typically more water-limited, higher temperatures and greater energy availability during the recovery phase may enhance photosynthetic capacity and metabolic activity once water is restored, promoting more efficient carbon assimilation and non-structural carbohydrate accumulation[47]. Warmer conditions may also facilitate the recovery of hydraulic function and leaf physiology after drought. Therefore, under warmer conditions, post-

drought rewetting may more effectively extend late-season carbon gain and increase carbon reserves available for subsequent growth, while potentially modifying the balance between chilling and forcing requirements that regulate spring phenology.

Mixed forests showed weaker phenological responses to post-drought rewetting than either deciduous or evergreen forests. This dampening effect in mixed forests likely stems from functional buffering[48,49], where the diversity of hydraulic strategies and phenological timings minimizes the community-level impact of individual dry-wet cycles. Species-level patterns further support a trait-based mechanism. Evergreen species responded more strongly than deciduous species, reflecting their conservative leaf economic strategy[50]. Their year-round carbon assimilation potential and greater drought tolerance allow them to exploit the rewetting window more effectively than deciduous trees that might already be starting to senesce, thereby extending opportunities for compensatory carbon assimilation that supports earlier spring reactivation[51–53].

Taken together, our findings highlight that phenological responses to post-drought rewetting are jointly modulated by climatic conditions, community structure, and species-specific functional traits. Accounting for this ecological heterogeneity will be essential for predicting phenological dynamics under increasingly variable hydroclimatic regimes. From a management perspective, maintaining species diversity and structural complexity may help buffer forest ecosystems against intensifying dry-wet variability by reducing the magnitude of phenological disruptions.

Future impacts of post-drought rewetting on tree phenology

Although increasing drought frequency and hydroclimatic variability are expected to intensify physiological stress and reduce forest productivity[18]. Recovery following drought release can stimulate compensatory carbon gain and partially offset drought-induced losses[27]. Our CMIP6 simulations suggest that post-drought rewetting may continue to advance subsequent spring phenology and delay autumn phenology through 2100 across emission scenarios. Simulated primary productivity further indicate that carbon assimilation responses to post-drought rewetting intensify with warming, with the largest increases projected under the high-emission SSP5-8.5 scenario. This pattern is consistent with stronger recovery under warmer conditions, where greater energy availability may promote photosynthetic recovery and carbohydrate accumulation once water becomes available. Although CMIP6 models project the persistence of this cross-seasonal pathway, these projections likely capture primarily its thermal component. Explicit representation of the biological overcompensation mechanism identified here could therefore enable more accurate projections of future ecosystem responses. Assessments that consider drought impacts alone may therefore overestimate long-term productivity losses by overlooking the overcompensatory effects of post-drought rewetting and recovery[54]. By enhancing late-season carbon gain and carbohydrate reserves, this overcompensatory recovery may sustain cross-seasonal phenological legacies and provide the carbon resources needed for earlier spring reactivation under future climate change.

Conclusion

By combining hemispheric-scale observations with controlled post-drought rewetting

experiments, we show that post-drought recovery can generate overcompensatory carbon gain with cross-seasonal consequences. Rewetting delayed autumn phenology and enhanced ecosystem productivity, thereby extending and increasing carbon acquisition during recovery. Experiments further revealed rapid restoration of photosynthetic capacity and greater nonstructural carbohydrate storage, particularly starch, providing carbon resources that persisted beyond the recovery season. This overcompensatory response carried over to advance subsequent spring phenology, with greater effects in warmer regions and evergreen species. CMIP6 projections suggest that these phenological legacies will persist through the twenty-first century as hydroclimatic variability intensifies. Our findings therefore recast post-drought recovery as an active overcompensatory phase that reorganizes carbon acquisition, storage and phenological development across seasons. Incorporating such recovery-driven legacies into phenology and ecosystem models may improve projections of forest resilience and carbon-cycle feedbacks under future climate change.

Methods

Ground-based phenology networks

Ground-based phenological observations were compiled from three regional phenological networks, including the Pan European Phenology Network (PEP725)[55], the Russian Chronicles of Nature Network (RCNN)[56], and the China Phenological Observation Network (CPON)[57]. Leaf-out or budburst and leaf coloration or leaf fall were used to represent spring and autumn phenology, respectively, hereafter referred to as the start of season (SOS) and end of season (EOS). These definitions were applied consistently across all networks, and all phenological dates were expressed as day of year (DOY).

To ensure biological plausibility, SOS records occurring after June and EOS records occurring before July were excluded. For each species–site combination, SOS and EOS records exceeding 2.5 times of median absolute deviation (MAD) were removed to further reduce the influence of potential outliers[58]. Only sites with more than five years of valid observations were retained for analysis. After filtering, the final dataset included 131,957 phenological records for 14 temperate tree species across 2,765 sites from 1982 to 2020 in PEP725, 7,232 records for 180 species across 137 sites from 1981 to 2016 in RCNN, and 5,235 records for 341 species across 37 sites from 1982 to 2017 in CPON.

Satellite-derived phenological products

GOSIF-GPP phenological product. The GOSIF-GPP product estimates global gross primary production from OCO-2-based solar-induced chlorophyll fluorescence, providing a physiologically meaningful proxy for canopy photosynthetic activity. Compared with greenness-based vegetation indices, GOSIF-GPP is more directly related to carbon assimilation and is therefore well suited for detecting phenological transitions in ecosystem productivity. Vegetation phenological metrics were extracted from the Global OCO-2 Solar-Induced Fluorescence-based Gross Primary Production dataset (GOSIF-GPP) at a spatial resolution of 0.05° for the period 2001–2020[59,60]. The GPP time series was first smoothed using a Savitzky–Golay filter[61], and phenological transitions were then detected using the Pruned Exact Linear Time (PELT) algorithm[62].

Spring and autumn transitions were identified as the points at which the smoothed GPP time series crossed amplitude thresholds of 10%, 15%, and 50%, where amplitude was defined as the difference between seasonal peak and baseline values within each growing cycle. We used the 50% threshold to define SOS and EOS, as it is less sensitive to noise[63], more consistent across sensors, and better aligned with ground-based observations.

MODIS-NBAR phenological product. The Terra and Aqua combined Moderate Resolution Imaging Spectroradiometer (MODIS) Land Cover Dynamics product (MCD12Q2, Version 6.1) provides global land surface phenology metrics at a spatial resolution of 500 m for the period 2001–2021[64]. This product is derived from time series of the two-band Enhanced Vegetation Index (EVI2), calculated from MODIS Nadir Bidirectional Reflectance Distribution Function (BRDF)-Adjusted Reflectance (NBAR). The 'MidGreenup' and 'MidGreendown' phases were used to define the start and end of the growing season, respectively. Specifically, SOS was identified as the date when EVI2 first exceeded 50% of the seasonal amplitude, and EOS as the date when EVI2 last fell below this threshold.

GIMMS NDVI3g phenological product. The Global Inventory Modeling and Mapping Studies third-generation NDVI dataset (GIMMS NDVI3g) provides long-term vegetation dynamics derived from Advanced Very High Resolution Radiometer (AVHRR) observations, spanning 1982–2014 at a spatial resolution of 0.08° and a temporal resolution of 15 days[65]. Pixels with an annual mean NDVI below 0.1 were excluded as non-vegetated areas. The NDVI time series was smoothed using a Savitzky–Golay filter prior to phenology extraction[66]. Phenological dates were determined using an inflection-point detection approach, in which a double logistic function (Eq. 1) was fitted to the NDVI time series, and the second derivative of the fitted curve was used to identify transition points[67]. SOS was defined as the first local maximum in curvature during the first half of the year, and EOS as the second local maximum during the second half.

$$y(t) = a + b\left(\frac{1}{1+e^{c(t-d)}} + \frac{1}{1+e^{e(t-f)}}\right) \quad (1)$$

where *c, d, e,* and *b* are parameters of the function, and *a* is the initial background NDVI value, $a + b$ is the maximum NDVI value, t is time in days, and $y(t)$ is the NDVI value at time t.

To ensure seasonal consistency, SOS dates occurring after June and EOS dates occurring before July were excluded across all three datasets. Only pixels with more than five years of valid observations were retained for subsequent analyses.

Future phenological data

Within the Coupled Model Intercomparison Project Phase 6 (CMIP6) framework, future GPP simulations were used as the basis for deriving future phenological metrics for 2021–2100 under four Shared Socioeconomic Pathway scenarios, including SSP1-2.6, SSP2-4.5, SSP3-7.0 and SSP5-8.5. We integrated projected phenological metrics and carbon productivity outputs derived from four models[68], including NorESM2-MM, CAS-ESM2-0, CMCC-ESM2-SR5, and CMCC-ESM2. For the NorESM2-MM model,

the GPP simulations were aggregated from 3-hourly to daily resolution, and the other three models used cubic spline interpolation for temporal sequence interpolation. Time series smoothing was performed using the Weighted Harmonic Analysis of Time Series (HANTS) method, a Fourier-based approach designed to characterize seasonal dynamics while reducing noise. The smoothed GPP curves were then fitted using the Elmore method to improve computational efficiency and phenological extraction accuracy[69–71].

Phenological transition dates were identified using three complementary algorithms. The derivative method (DER) defined SOS and EOS as the dates of maximum change during the ascending and descending phases of the GPP curve, respectively[72]. The Gu method (RD) identified SOS and EOS by fitting tangent lines to the seasonal curve and determining their intersections with the seasonal baseline[73]. The 50% threshold method (TRS5) defined SOS and EOS as the dates when GPP reached 50% of the seasonal amplitude during the ascending and descending phases, respectively[74,75]. The DER was used as the primary approach, whereas the RD and TRS5 were used as independent validations to assess algorithmic robustness. Only pixels with more than five years of valid phenological estimates were retained for subsequent trend analyses.

Photosynthetic productivity data

We used three sets of gross primary productivity (GPP) and net primary productivity (NPP) data as proxies for vegetation photosynthetic productivity, matched to the corresponding phenological products.

For the MODIS-NBAR phenology product, GPP and NPP were obtained from the MOD17A2H Version 6.1 product, produced by the Numerical Terradynamic Simulation Group (NTSG) at the University of Montana[76]. This product has a spatial resolution of 500 m and an 8-day temporal resolution. MOD17A2H is based on a light use efficiency model and is widely used to monitor terrestrial carbon cycle dynamics. The data were processed in Google Earth Engine following the product user guide, and the original 8-day composites were aggregated to monthly and annual values using weighted averaging.

For the GOSIF-GPP and GIMMS NDVI3g phenology products, annual GPP and NPP data for 1982–2018 were obtained from the Global Land Surface Satellite (GLASS) products at a spatial resolution of 0.05°[77]. The GLASS GPP product is generated using the revised Eddy Covariance–Light Use Efficiency model, whereas GLASS NPP is estimated by combining GLASS GPP with the ratio of autotrophic respiration to GPP derived from dynamic vegetation models in the TRENDY ensemble.

For future phenological analyses, monthly GPP and NPP projections for 2021–2100 were obtained from corresponding models (NorESM2-MM, CAS-ESM2-0, CMCC-ESM2-SR5, and CMCC-ESM2) at a spatial resolution of 1° under four SSP scenarios (https://esgf-node.llnl.gov/projects/esgf-llnl/). These simulations were generated within the CMIP6 framework and provide projections of future vegetation productivity and carbon-cycle feedbacks under different climate change pathways.

Climate data and vegetation type classification

Daily temperature at a spatial resolution of 0.1° was obtained from the ERA5-Land reanalysis dataset and used to calculate mean annual temperature (MAT)[78]. Drought conditions were characterized using the Standardized Precipitation Evapotranspiration Index (SPEI), a widely used multi-timescale drought index that captures climatic water balance across different temporal windows. We used historical and future 3-month SPEI (SPEI-3), as it integrates cumulative moisture anomalies over a seasonal timescale relevant to tree physiological recovery while bridging transient weather fluctuations and longer-term hydrological variability[79,80]. Historical SPEI-3 data at 0.05° spatial resolution were obtained from the Hydro-JULES global drought dataset[81], whereas future SPEI-3 projections at 0.25° spatial resolution were derived from corresponding models for 2021–2100 under four SSP scenarios (SSP1-2.6, SSP2-4.5, SSP3-7.0 and SSP5-8.5)[82].

Vegetation type for each pixel and study site was classified using the International Geosphere–Biosphere Programme (IGBP) scheme[83] based on the MODIS land cover product MCD12Q1, which provides 17 land-cover classes at 500 m spatial resolution[64]. Tropical forests and non-forest vegetation types were excluded, and the study domain was restricted to latitudes north of 30° N, where seasonal phenological cycles are well defined and climatologically meaningful[84]. The remaining forest classes were reclassified into three functional types: deciduous, evergreen and mixed forests.

To ensure spatial consistency among datasets with different native resolutions, all datasets were resampled to a common grid. Historical phenology products, SPEI data and land-cover data were resampled to 0.1° to match the ERA5-Land climate variables, whereas future SPEI data were resampled to 1° to align with the CMIP6 outputs. All phenology datasets were converted from raster to point format to enable site-, species- and pixel-level analyses. Environmental variables for each site or pixel were extracted using the *terra* package[85] in R.

Controlled post-drought rewetting experiment

Plant materials and experimental design

The post-drought rewetting experiment was conducted at the Pengzhou Experimental Research Station in Sichuan, China (31°10′N, 104°00′E), a region characterized by a subtropical monsoon climate, with mean annual air temperatures ranging from 14 to 23 °C and mean annual precipitation of 1,093 mm in 2024. Four native tree species were selected, including two deciduous species, *Camptotheca acuminata* Decne. and *Metasequoia glyptostroboides* Hu & W.C. Cheng, and two evergreen species, *Quercus glauca* Thunb. and *Cunninghamia lanceolata* (Lamb.) Hook.

Two-year-old seedlings were obtained from a nearby nursery and screened to ensure uniformity in size and health status. Selected individuals were transplanted into plastic pots (24 cm in diameter and 24.3 cm in depth) filled with a 1:1 (v/v) mixture of native topsoil and commercial substrate composed of peat, vermiculite and perlite. After transplantation, the substrate was thoroughly watered with a solution containing fungicide and rooting hormone to facilitate establishment in December 2023. Seedlings were then maintained under standard nursery conditions for three months prior to the post-drought rewetting treatments, which began in March 2024.

Seedlings were randomly assigned to two treatment groups: constant-wetting (CW) and post-drought rewetting (DRW). From May to August 2024, CW were maintained at 70–90% of field capacity through weekly irrigation, whereas drought was imposed in DRW by reducing irrigation relative to the control and dynamically adjusting water supply according to soil moisture sensor readings to maintain soil water content at 40–60% of field capacity[86,87]. Rewetting was initiated in September 2024, when irrigation in the DRW treatment was restored to the CW level to maintain soil water content at 70–90% of field capacity. Soil temperature and moisture were continuously recorded at 5-min intervals in both treatments using data loggers (S21A, Pengyun, China).

Phenological monitoring and physiological measurements

For each species, eight seedlings per treatment were monitored for phenological development from March 2024 to April 2025. For both deciduous and evergreen species, SOS was defined as the date of leaf unfolding, whereas EOS was defined as the date of leaf coloration in deciduous species and bud set in evergreen species.

Healthy and relatively uniform seedlings were selected for non-structural carbohydrate (NSC) analyses to trace carbon dynamics under CW and DRW treatments. Destructive sampling was conducted during the drought-stress and rewetting phases. Samples were oven-dried at 105 °C for 30 min and then at 65 °C until constant weight. Dried tissues were weighed and ground using a tissue grinder (V4800, China) for subsequent analyses. Soluble sugar and starch concentrations were quantified using commercial kits (BC0035 and BC0705, Solarbio, China) following the manufacturer's protocols[88]. Total NSC concentration was calculated as the sum of soluble sugar and starch concentrations.

Total chlorophyll concentration, used as a proxy for photosynthetic capacity, was determined from fresh leaf discs extracted with 95% (v/v) ethanol in the dark at 4 °C for 24 h until complete bleaching. After that, the absorbance of extracted solution was recorded spectrophotometrically using a spectrophotometer (Multiskan FC Microplate Photometer, Thermo Fisher, USA) at an absorbance of 649 nm and 665 nm, based on the equations used for Chl a and Chl b calculations[89].

Statistical analyses

Identification of post-drought rewetting events

In this study, we used SPEI-3 to identify short-term and seasonal drought events, defined as periods when SPEI-3 fell below −1[90]. Based on monthly SPEI-3 and phenology data, we identified continuous-wetting (CW) and post-drought rewetting (DRW) events. First, the growing season for each year was defined from SOS to EOS. Second, DRW events were identified when SPEI-3 fell below −1 at least once between SOS and two months before EOS and then exceeded −1 during both the EOS month and the preceding month. Third, CW events were defined in which SPEI-3 remained consistently above −1 throughout the growing season.

Effects of post-drought rewetting on phenology

We first compared SOS_{next} and $EOS_{current}$ between DRW and CW to investigate the effects of DRW on phenology using three ground-based phenological datasets (PEP725, RCNN, and CPON) across the Northern Hemisphere. Because PEP725 provides the broadest spatial coverage and longest temporal record among the four ground-based datasets, we used it to examine species-specific phenological responses in four widespread European tree species, *Aesculus hippocastanum* L., *Betula pendula* Roth., *Fagus sylvatica* L. and *Quercus robur* L. To examine spatial variation in phenological responses, pixels from the three satellite-derived datasets were classified into warm and cold regions based on the long-term median MAT value. Meanwhile, vegetation was categorized into deciduous, evergreen, and mixed forests to account for differences in phenological characteristics among plant functional types. Phenological differences between DRW and CW conditions were then compared across thermal regions and forest types.

The two-tailed *t*-test was used to assess differences between DRW and CW. To test the robustness of the results, we further fitted linear mixed-effects models using the *lmerTest* package[91] in R. In each model, phenological timing was specified as the response variable and modeled as a function of treatment, group and their interaction, with pixel included as a random intercept. Because phenological curve fitting introduces estimation uncertainty in both SOS_{next} and $EOS_{current}$, we further examined their relationship following post-drought rewetting using standardized major axis (SMA) regression, which treats the two variables symmetrically and accounts for variation in both[92], unlike ordinary least-squares regression. SMA analyses were performed using the R package *smatr*[93].

Effect of post-drought rewetting on productivity

We quantified pixel-level differences in mean annual GPP and NPP between DRW and CW conditions across the three satellite-derived datasets, denoting as ΔGPP and ΔNPP, and calculated the percentage of pixels showing positive or negative. Moreover, we paired forest productivity metrics with concurrent phenological records and quantified their relationships using SMA regressions. Using the controlled post-drought rewetting experiment, we further assessed the effects of DRW on NSC and chlorophyll concentrations. Differences in starch, soluble sugar, total NSC and total chlorophyll concentrations between CW and DRW treatments were tested using two-tailed *t*-tests. To evaluate the potential role of NSCs in mediating phenological responses, we examined relationships between NSC concentrations and spring or autumn phenological timing using linear regression.

We further used structural equation modelling (SEM) to examine relationships among $EOS_{current}$, NSC concentrations and SOS_{next} in the controlled post-drought rewetting experiment. The SEM included both direct and indirect pathways linking DRW to phenological responses. Specifically, we hypothesized that DRW directly affects SOS_{next} and indirectly affects it by delaying $EOS_{current}$, increasing NSC concentrations and ultimately advancing SOS_{next}. Additional direct paths from DRW to NSC concentrations and from $EOS_{current}$ to SOS_{next} were also included. SEM was fitted using the *piecewiseSEM* package[94] in R. Path coefficients were estimated using maximum likelihood. Direct, indirect and total effects were quantified, with total effects calculated as the sum of direct and indirect pathways. Bootstrap resampling with 1,000 iterations

was used to estimate robust 95% confidence intervals for path coefficients from the *boot* package[95] in R.

Future post-drought rewetting effects on phenology and productivity

To assess future changes in phenology and forest productivity, we extracted phenological and productivity metrics from simulations by four CMIP6 models under four SSP scenarios, SSP1–2.6, SSP2–4.5, SSP3–7.0 and SSP5–8.5, and calculated ensemble means to reduce uncertainty associated with intermodel variability. DRW and CW events were identified using the same criteria as in the historical analyses to ensure consistency. The 80-year projection period was divided into four 20-year intervals, 2021–2040, 2041–2060, 2061–2080 and 2081–2100, to capture multi-decadal variation in climate and phenological responses. To assess the effects of DRW under future climate change, we compared projected SOS_{next} and $EOS_{current}$ between DRW and CW across time intervals and scenarios. We further calculated pixel-level mean differences in future GPP and NPP between DRW and CW, expressed as ΔGPP and ΔNPP, and quantified the percentage of pixels showing positive or negative during 2021–2100 under each SSP scenario.

All statistical analyses were performed in R version 4.4.2[96].

Data availability

The data that support the findings of this study are derived from the following resources. The PEP725 phenological data was obtained from http://www.pep725.eu. RCNN data was downloaded from https://doi.org/10.1038/s41597-020-0376-z. CPON data was accessed from http://www.cpon.ac.cn. Remote sensing phenological products sourced included GOSIF-GPP (https://doi.org/10.6084/m9.figshare.17195009.v3), MODIS-NBAR (https://lpdaac.usgs.gov/), and GIMMS NDVI3g phenological product (https://globalecology.unh.edu/). MODIS GPP and NPP data are available at https://lpdaac.usgs.gov/products/mod17a2hv006/, GLASS GPP and NPP data are available at http://www.glass.umd.edu/index.html. Historical daily temperature was from ERA5-Land at https://cds.climate.copernicus.eu/datasets/derived-era5-land-daily-statistics, and historical monthly SPEI-3 was from Hydro-JULES global drought dataset at https://data.ceda.ac.uk/badc/hydro-jules/data/CHIRP-GLEAMS-amendment-2024/CHIRPS_GLEAM/. Land cover data were obtained from https://lpdaac.usgs.gov/products/mcd12q1v061. Future phenological projections were at https://www.geodata.cn/. Future monthly SPEI03 data was from https://ciesin.columbia.edu/content/data. Future monthly GPP and NPP data were at https://esgf-node.llnl.gov/projects/esgf-llnl/. The experimental data and demo datasets have been deposited in Zenodo (https://doi.org/10.5281/zenodo.22898144).

Code availability

The R scripts for statistical analyses and visualizations are available on Zenodo (https://doi.org/10.5281/zenodo.22898144).

References

1. Richardson, A. D. *et al.* Climate change, phenology, and phenological control of vegetation feedbacks to the climate system. *Agric. For. Meteorol.* **169**, 156–173 (2013).
2. Cleland, E. E. & Wolkovich, E. M. Effects of Phenology on Plant Community Assembly and Structure. *Annu. Rev. Ecol. Evol. Syst.* **55**, 471–492 (2024).
3. Keenan, T. F. *et al.* Net carbon uptake has increased through warming-induced changes in temperate forest phenology. *Nat. Clim. Change* **4**, 598–604 (2014).
4. Xia, J. *et al.* Joint control of terrestrial gross primary productivity by plant phenology and physiology. *Proc. Natl. Acad. Sci.* **112**, 2788–2793 (2015).
5. Richardson, A. D. *et al.* Influence of spring and autumn phenological transitions on forest ecosystem productivity. *Philos. Trans. R. Soc. B: Biol. Sci.* **365**, 3227–3246 (2010).
6. Peñuelas, J., Rutishauser, T. & Filella, I. Phenology Feedbacks on Climate Change. *Science* **324**, 887–888 (2009).
7. Jeong, S.-J., Ho, C.-H., Gim, H.-J. & Brown, M. E. Phenology shifts at start vs. end of growing season in temperate vegetation over the Northern Hemisphere for the period 1982–2008. *Global Change Biol.* **17**, 2385–2399 (2011).
8. Chen, S. *et al.* Vegetation phenology and its ecohydrological implications from individual to global scales. *Geogr. Sustainability* **3**, 334–338 (2022).
9. Drought hinders the advance of spring phenology through ecosystem memory effects. *Nat. Clim. Change* **15**, 362–363 (2025).
10. Richardson, A. D. *et al.* Climate change, phenology, and phenological control of vegetation feedbacks to the climate system. *Agric. For. Meteorol.* **169**, 156–173 (2013).
11. Meng, L. *et al.* Photoperiod decelerates the advance of spring phenology of six deciduous tree species under climate warming. *Global Change Biol.* **27**, 2914–2927 (2021).
12. Richardson, A. D. *et al.* Terrestrial biosphere models need better representation of vegetation phenology: results from the North American Carbon Program Site Synthesis. *Global Change Biol.* **18**, 566–584 (2012).
13. Piao, S. *et al.* Plant phenology and global climate change: Current progresses and challenges. *Global Change Biol.* **25**, 1922–1940 (2019).
14. Chuine, I. A Unified Model for Budburst of Trees. *J. Theor. Biol.* **207**, 337–347 (2000).
15. Ettinger, A. K. *et al.* Winter temperatures predominate in spring phenological responses to warming. *Nat. Clim. Change* **10**, 1137–1142 (2020).
16. Amico Roxas, A., Orozco, J., Guzmán-Delgado, P. & Zwieniecki, M. A. Spring phenology is affected by fall non-structural carbohydrate concentration and winter sugar redistribution in three mediterranean nut tree species. *Tree Physiol.* **41**, 1425–1438 (2021).
17. Gu, H. *et al.* Warming-induced increase in carbon uptake is linked to earlier spring phenology in temperate and boreal forests. *Nat. Commun.* **13**, 3698 (2022).
18. Reichstein, M. *et al.* Climate extremes and the carbon cycle. *Nature* **500**, 287–295

(2013).
19. von Buttlar, J. *et al.* Impacts of droughts and extreme-temperature events on gross primary production and ecosystem respiration: A systematic assessment across ecosystems and climate zones. *Biogeosciences* **15**, 1293–1318 (2018).
20. Wang, W., Peng, C., Kneeshaw, D. D., Larocque, G. R. & Luo, Z. Drought-induced tree mortality: ecological consequences, causes, and modeling. *Environ. Rev.* **20**, 109–121 (2012).
21. Chambers, J. Q. *et al.* Hot droughts in the Amazon provide a window to a future hypertropical climate. *Nature* **649**, 1190–1196 (2026).
22. McDowell, N. *et al.* Mechanisms of plant survival and mortality during drought: why do some plants survive while others succumb to drought? *New Phytol.* **178**, 719–739 (2008).
23. Thompson, R. A. *et al.* No carbon storage in growth-limited trees in a semi-arid woodland. *Nat. Commun.* **14**, 1959 (2023).
24. Adams, H. D. *et al.* A multi-species synthesis of physiological mechanisms in drought-induced tree mortality. *Nat. Ecol. Evol.* **1**, 1285–1291 (2017).
25. Min, S.-K., Zhang, X., Zwiers, F. W. & Hegerl, G. C. Human contribution to more-intense precipitation extremes. *Nature* **470**, 378–381 (2011).
26. Seneviratne, S. I. *et al.* Weather and climate extreme events in a changing climate. in *Climate Change 2021: The Physical Science Basis: Working Group I contribution to the Sixth Assessment Report of the Intergovernmental Panel on Climate Change* (eds Masson-Delmotte, V. P., Zhai, A., Pirani, S. L. & Connors, C.) 1513–1766 (Cambridge University Press, Cambridge, UK, 2021).
27. Jiang, P. *et al.* Enhanced growth after extreme wetness compensates for post-drought carbon loss in dry forests. *Nat. Commun.* **10**, 195 (2019).
28. Ru, J., Wan, S., Hui, D. & Song, J. Overcompensation of ecosystem productivity following sustained extreme drought in a semiarid grassland. *Ecology* **104**, e3997 (2023).
29. Unger, S., Máguas, C., Pereira, J. S., David, T. S. & Werner, C. Interpreting post-drought rewetting effects on soil and ecosystem carbon dynamics in a Mediterranean oak savannah. *Agric. For. Meteorol.* **154–155**, 9–18 (2012).
30. Ruehr, N. K., Grote, R., Mayr, S. & Arneth, A. Beyond the extreme: recovery of carbon and water relations in woody plants following heat and drought stress. *Tree Physiol.* **39**, 1285–1299 (2019).
31. Li, Y. *et al.* Widespread spring phenology effects on drought recovery of Northern Hemisphere ecosystems. *Nat. Clim. Change* **13**, 182–188 (2023).
32. Beil, I., Kreyling, J., Meyer, C., Lemcke, N. & Malyshev, A. V. Late to bed, late to rise—Warmer autumn temperatures delay spring phenology by delaying dormancy. *Global Change Biol.* **27**, 5806–5817 (2021).
33. Wu, Z. *et al.* Carry-over effects between spring and autumn phenology differ among the world's biomes. *Natl. Sci. Rev.* **13**, nwag082 (2026).
34. Shen, M. *et al.* Can changes in autumn phenology facilitate earlier green-up date of northern vegetation? *Agric. For. Meteorol.* **291**, 108077 (2020).
35. Luo, Y. *et al.* Internal physiological drivers of leaf development in trees:

Understanding the relationship between non-structural carbohydrates and leaf phenology. *Funct. Ecol.* **40**, 1151–1164 (2026).
36. Tixier, A., Gambetta, G. A., Godfrey, J., Orozco, J. & Zwieniecki, M. A. Non-structural carbohydrates in dormant woody perennials; the tale of winter survival and spring arrival. *Front. For. Global Change* **2**, (2019).
37. Klein, T., Vitasse, Y. & Hoch, G. Coordination between growth, phenology and carbon storage in three coexisting deciduous tree species in a temperate forest. *Tree Physiol.* **36**, 847–855 (2016).
38. Wang, J. *et al.* Late spring frost delays tree spring phenology by reducing photosynthetic productivity. *Nat. Clim. Change* **15**, 201–209 (2025).
39. Liu, Y. *et al.* Drought legacies delay spring green-up in northern ecosystems. *Nat. Clim. Change* **15**, 444–451 (2025).
40. Zani, D., Crowther, T. W., Mo, L., Renner, S. S. & Zohner, C. M. Increased growing-season productivity drives earlier autumn leaf senescence in temperate trees. *Science* **370**, 1066–1071 (2020).
41. Singini, E. J. & Drew, D. Asynchronous recovery of water relations and photosynthesis following natural rainfall pulses in eucalyptus. *Tree Physiol.* **46**, tpag016 (2026).
42. Pflug, E. E. *et al.* Resilient leaf physiological response of european beech (fagus sylvatica L.) to summer drought and drought release. *Front. Plant Sci.* **9**, (2018).
43. Zlobin, I. E. *et al.* Abscisic acid and cytokinins are not involved in the regulation of stomatal conductance of scots pine saplings during post-drought recovery. *Biomolecules* **13**, 523 (2023).
44. Zhang, Y., Yang, Q., Lee, D. W., Goldstein, G. & Cao, K. Extended leaf senescence promotes carbon gain and nutrient resorption: Importance of maintaining winter photosynthesis in subtropical forests. *Oecologia* **173**, 721–730 (2013).
45. Estiarte, M. & Peñuelas, J. Alteration of the phenology of leaf senescence and fall in winter deciduous species by climate change: Effects on nutrient proficiency. *Global Change Biol.* **21**, 1005–1017 (2015).
46. Kannenberg, S. A., Schwalm, C. R. & Anderegg, W. R. L. Ghosts of the past: How drought legacy effects shape forest functioning and carbon cycling. *Ecol. Lett.* **23**, 891–901 (2020).
47. Shi, C. *et al.* Climate warming alters nitrogen dynamics and total non-structural carbohydrate accumulations of perennial herbs of distinctive functional groups during the plant senescence in autumn in an alpine meadow of the tibetan plateau, China. *Agric. For. Meteorol.* **200**, 21–29 (2015).
48. Isbell, F. *et al.* Biodiversity increases the resistance of ecosystem productivity to climate extremes. *Nature* **526**, 574–577 (2015).
49. Zhang, T., Di, D., Liao, X. & Shi, W. Response of forest plant diversity to drought: A review. *Water* **15**, 3486 (2023).
50. Wright, I. J. *et al.* The worldwide leaf economics spectrum. *Nature* **428**, 821–827 (2004).
51. van Ommen Kloeke, A. E. E., Douma, J. C., Ordoñez, J. C., Reich, P. B. & van Bodegom, P. M. Global quantification of contrasting leaf life span strategies for

deciduous and evergreen species in response to environmental conditions. *Global Ecol. Biogeogr.* **21**, 224–235 (2012).
52. Ye, Y., Kitayama, K. & Onoda, Y. A cost–benefit analysis of leaf carbon economy with consideration of seasonal changes in leaf traits for sympatric deciduous and evergreen congeners: Implications for their coexistence. *New Phytol.* **234**, 1047–1058 (2022).
53. Photosynthetic limitation and mechanisms of photoprotection under drought and recovery of calotropis procera, an evergreen C3 from arid regions. *Plant Physiol. Biochem.* **118**, 589–599 (2017).
54. Ovenden, T. S., Perks, M. P., Clarke, T.-K., Mencuccini, M. & Jump, A. S. Life after recovery: Increased resolution of forest resilience assessment sheds new light on post-drought compensatory growth and recovery dynamics. *J. Ecol.* **109**, 3157–3170 (2021).
55. Templ, B. *et al.* Pan European Phenological database (PEP725): a single point of access for European data. *Int. J. Biometeorol.* **62**, 1109–1113 (2018).
56. Ovaskainen, O. *et al.* Chronicles of nature calendar, a long-term and large-scale multitaxon database on phenology. *Sci. Data* **7**, 47 (2020).
57. Ge, Q., Wang, H., Rutishauser, T. & Dai, J. Phenological response to climate change in China: a meta-analysis. *Global Change Biol.* **21**, 265–274 (2015).
58. Leys, C., Ley, C., Klein, O., Bernard, P. & Licata, L. Detecting outliers: Do not use standard deviation around the mean, use absolute deviation around the median. *J. Exp. Soc. Psychol.* **49**, 764–766 (2013).
59. Fang, J. *et al.* Vegetation photosynthetic phenology dataset in northern terrestrial ecosystems. *Sci. Data* **10**, 300 (2023).
60. Li, X. & Xiao, J. A Global, 0.05-Degree Product of Solar-Induced Chlorophyll Fluorescence Derived from OCO-2, MODIS, and Reanalysis Data. *Remote Sens.* **11**, 517 (2019).
61. Chen, J. *et al.* A simple method for reconstructing a high-quality NDVI time-series data set based on the Savitzky–Golay filter. *Remote Sens. Environ.* **91**, 332–344 (2004).
62. Killick, R., Fearnhead, P. & Eckley, I. A. Optimal Detection of Changepoints With a Linear Computational Cost. *J. Am. Stat. Assoc.* **107**, 1590–1598 (2012).
63. Richardson, A. D. *et al.* Tracking vegetation phenology across diverse North American biomes using PhenoCam imagery. *Sci. Data* **5**, 180028 (2018).
64. Friedl, M. A., Gray, J. & Sulla-Menashe, D. MODIS/Terra+Aqua Land Cover Dynamics Yearly L3 Global 500m SIN Grid V061. NASA Land Processes Distributed Active Archive Center https://doi.org/10.5067/MODIS/MCD12Q2.061 (2022).
65. Pinzon, J. E. & Tucker, C. J. A non-stationary 1981–2012 AVHRR NDVI3g time series. *Remote Sens.* **6**, 6929–6960 (2014).
66. Wang, X. *et al.* Validation of MODIS-GPP product at 10 flux sites in northern China. *Int. J. Remote Sens.* **34**, 587–599 (2013).
67. Wang, X. *et al.* No trends in spring and autumn phenology during the global warming hiatus. *Nat. Commun.* **10**, 2389 (2019).

68. Shen, P. *et al.* Biodiversity buffers the response of spring leaf unfolding to climate warming. *Nat. Clim. Change* **14**, 863–868 (2024).
69. Yang, G., Shen, H., Zhang, L., He, Z. & Li, X. A Moving Weighted Harmonic Analysis Method for Reconstructing High-Quality SPOT VEGETATION NDVI Time-Series Data. *IEEE Trans. Geosci. Remote Sens.* **53**, 6008–6021 (2015).
70. Bush, E. R. *et al.* Fourier analysis to detect phenological cycles using long-term tropical field data and simulations. *Methods Ecol. Evol.* **8**, 530–540 (2017).
71. Elmore, A. J., Guinn, S. M., Minsley, B. J. & Richardson, A. D. Landscape controls on the timing of spring, autumn, and growing season length in mid-Atlantic forests. *Global Change Biol.* **18**, 656–674 (2012).
72. Zhang, Q., Kong, D., Shi, P., Singh, V. P. & Sun, P. Vegetation phenology on the Qinghai-Tibetan Plateau and its response to climate change (1982–2013). *Agric. For. Meteorol.* **248**, 408–417 (2018).
73. Gu, L. *et al.* Characterizing the Seasonal Dynamics of Plant Community Photosynthesis Across a Range of Vegetation Types. in *Phenology of Ecosystem Processes: Applications in Global Change Research* (ed. Noormets, A.) 35–58 (Springer, New York, NY, 2009).
74. White, M. A., Running, S. W. & Thornton, P. E. The impact of growing-season length variability on carbon assimilation and evapotranspiration over 88 years in the eastern US deciduous forest. *Int. J. Biometeorol.* **42**, 139–145 (1999).
75. Shen, M. *et al.* Increasing altitudinal gradient of spring vegetation phenology during the last decade on the Qinghai–Tibetan Plateau. *Agric. For. Meteorol.* **189–190**, 71–80 (2014).
76. Running, S. W., Mu, Q. & Zhao, M. MODIS/Terra Gross Primary Productivity 8-Day L4 Global 500m SIN Grid V061. NASA Land Processes Distributed Active Archive Center https://doi.org/10.5067/MODIS/MOD17A2H.061 (2021).
77. Zheng, Y. *et al.* Improved estimate of global gross primary production for reproducing its long-term variation, 1982–2017. *Earth Syst. Sci. Data* **12**, 2725–2746 (2020).
78. ERA5-Land post-processed daily statistics from 1950 to present. Copernicus Climate Change Service (C3S) Climate Data Store (CDS) https://doi.org/10.24381/cds.e9c9c792 (2024).
79. He, Y. *et al.* Differential vegetation drought adaptability in global karst areas. *npj Clim. Atmos. Sci.* **8**, 343 (2025).
80. Marchand, W., Depardieu, C., Campbell, E. M., Bousquet, J. & Girardin, M. P. Long-term temporal divergence in post-drought resilience decline between deciduous and evergreen tree species. *Global Change Biol.* **31**, e70330 (2025).
81. Gebrechorkos, S. H. *et al.* Global high-resolution drought indices for 1981–2022. *Earth Syst. Sci. Data* **15**, 5449–5466 (2023).
82. Araujo, D. S. A. *et al.* Global future drought layers based on downscaled CMIP6 models and multiple socioeconomic pathways. *Sci. Data* **12**, 295 (2025).
83. Loveland, T. R. & Belward, A. S. The International Geosphere Biosphere Programme Data and Information System global land cover data set (DISCover). *Acta Astronaut.* **41**, 681–689 (1997).

84. *Phenology: An Integrative Environmental Science*. (Springer Netherlands, Dordrecht, 2013).
85. Hijmans, R. J. *et al.* terra: Spatial Data Analysis. https://doi.org/10.32614/CRAN.package.terra (2026).
86. Huang, X. *et al.* Effects of Drought Stress on Non-Structural Carbohydrates in Different Organs of Cunninghamia lanceolata. *Plants* **12**, (2023).
87. Liu, D. *et al.* Plasticity of physiological, anatomical and structural traits defines seedling growth during sustained drought. *Tree Physiol.* **45**, tpaf103 (2025).
88. Zhao, Y. *et al.* Photosynthetic characteristics and genetic mapping of a yellow-green leaf mutant jym165 in soybean. *BMC Plant Biol.* **24**, 1009 (2024).
89. Minocha, R., Martinez, G., Lyons, B. & Long, S. Development of a standardized methodology for quantifying total chlorophyll and carotenoids from foliage of hardwood and conifer tree species. *Can. J. For. Res.* **39**, 849–861 (2009).
90. Gebrechorkos, S. H. *et al.* Warming accelerates global drought severity. *Nature* **642**, 628–635 (2025).
91. Kuznetsova, A., Brockhoff, P. B. & Christensen, R. H. B. lmerTest package: Tests in linear mixed effects models. *J. Stat. Softw.* **82**, 1–26 (2017).
92. Warton, D. I., Wright, I. J., Falster, D. S. & Westoby, M. Bivariate line-fitting methods for allometry. *Biol. Rev.* **81**, 259–291 (2006).
93. Warton, D. I., Duursma, R. A., Falster, D. S. & Taskinen, S. smatr 3– an R package for estimation and inference about allometric lines. *Methods Ecol. Evol.* **3**, 257–259 (2012).
94. Lefcheck, J. S. piecewiseSEM: Piecewise structural equation modelling in r for ecology, evolution, and systematics. *Methods Ecol. Evol.* **7**, 573–579 (2016).
95. Davison, A. C. & Hinkley, D. V. *Bootstrap Methods and Their Application*. (Cambridge University Press, Cambridge, 1997).
96. R Core Team. R: A language and environment for statistical computing. (2024).

Acknowledgements

We acknowledge all members of the PEP 725 network, USA-NPN, CPON, and RCNN for collecting and providing phenological data. Special thanks go to the members of the phenology research group for their invaluable support and assistance with the experiment.

Funding

The National Key R&D Program of China (2023YFF0806600) and the National Natural Science Foundation of China (32271833).

Author contributions

L.C. conceived and designed the research. M.Y., Y.J., J.L., and H.G. collected the data with the inputs from X.W., H.Q., A.Y., G.B., Q.Y., J.M.., and Y.M. Y.J. and J.L. performed the data analyses and produced the figures with the inputs of X.W., H.G., and M.Y. Y.J. wrote the first draft with the inputs from L.C., X.W., H.G., H.Q., A.Y., G.B., Q.Y., J.M., and J.P. All authors discussed the design and methodology and contributed to the interpretation of the results and approved the final manuscript.

Ethics declarations

Competing interests

The authors declare no competing interests.

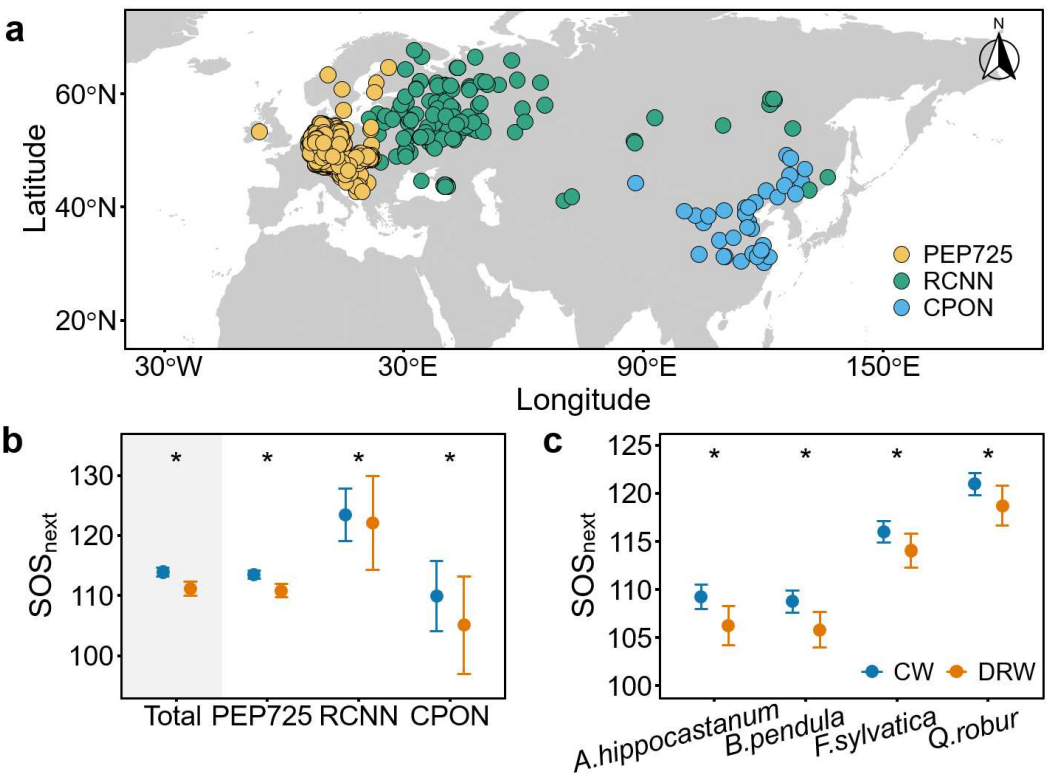


Fig. 1 Site distribution and the effects of post-drought rewetting on the timing of spring phenology of next year across ground-based phenological networks. a, Geographical distribution of the phenological observation sites in the study. Yellow, green, and blue dots represent sites from PEP725, RCNN, and CPON networks, respectively. **b,** Differences in the start of growing season in the next year (SOS_{next}) between constant-wetting (CW) and post-drought rewetting (DRW) across three phenological networks. **c**, Differences in SOS_{next} between CW and DRW for four representative European tree species (*Aesculus hippocastanum*, *Betula pendula*, *Fagus sylvatica*, and *Quercus robur*) from the PEP725 network. In **b**–**c**, points represent mean day of year (DOY) and error bars show 10 times the 95% confidence intervals. The asterisk indicates a significant difference (two-tailed *t*-test, $P < 0.05$).

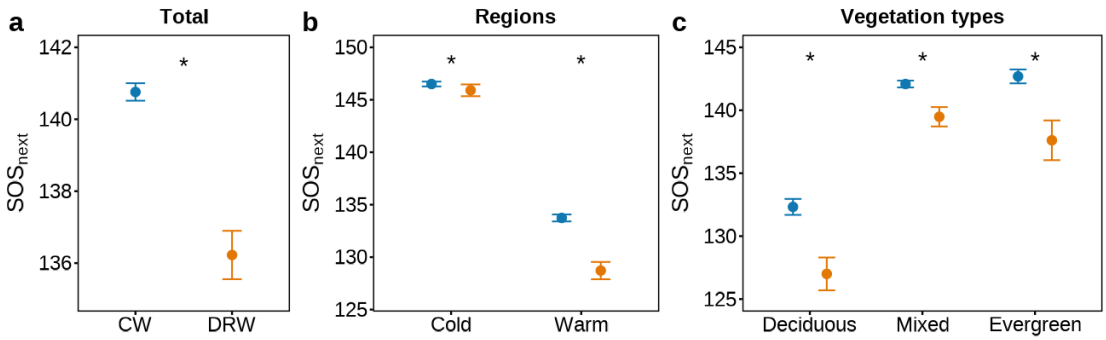


Fig. 2 Effects of post-drought rewetting on the timing of spring phenology based on GOSIF-GPP phenological products. Differences in the start of growing season in the next year (SOS_{next}) between constant-wetting (CW) and post-drought rewetting (DRW) across the total dataset (**a**), regions (**b**), and vegetation types (**c**). Pixels were classified into cold and warm regions based on the long-term mean temperatures, and deciduous, mixed, and evergreen based on their forest types. In **a**–**c**, points represent mean day of year (DOY) and error bars show 10 times the 95% confidence intervals. The asterisk indicates a significant difference (two-tailed *t*-test, $P < 0.05$).

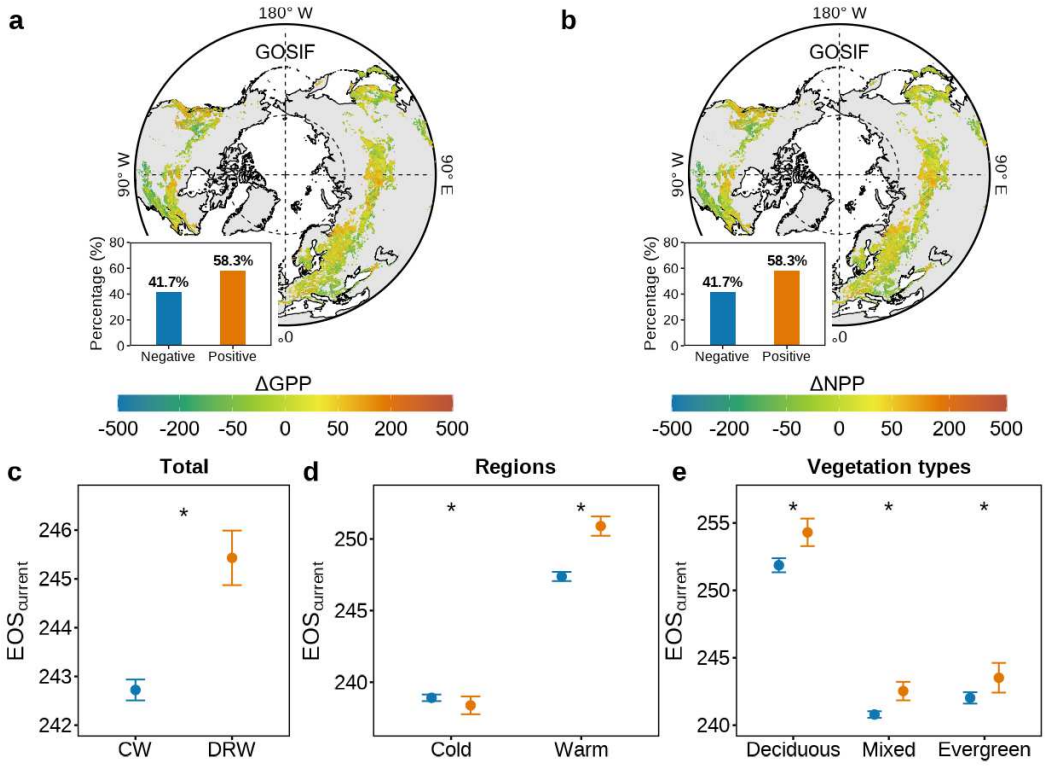


Fig. 3 Effects of post-drought rewetting on forest gross primary productivity (GPP), net primary production (NPP), and the timing of autumn phenology based on GOSIF-GPP phenological products. a–**b**, Differences in GPP (**a**) and NPP (**b**) between constant-wetting (CW) and post-drought rewetting (DRW) across the Northern Hemisphere forests. **c**–**e**, Differences in the end of growing season in the current year ($EOS_{current}$) between CW and DRW across the total dataset (**c**), regions (**d**), and vegetation types (**e**). Insets in (**a**) and (**b**) show the percentages of negative (blue) or positive (yellow) value of difference. In **c**–**d**, pixels were classified into cold and warm based on the long-term mean temperatures, and deciduous, mixed, and evergreen based on their forest types. Points represent mean day of year (DOY) and error bars show 10 times the 95% confidence intervals. The asterisk indicates a significant difference (two-tailed *t*-test, $P < 0.05$).

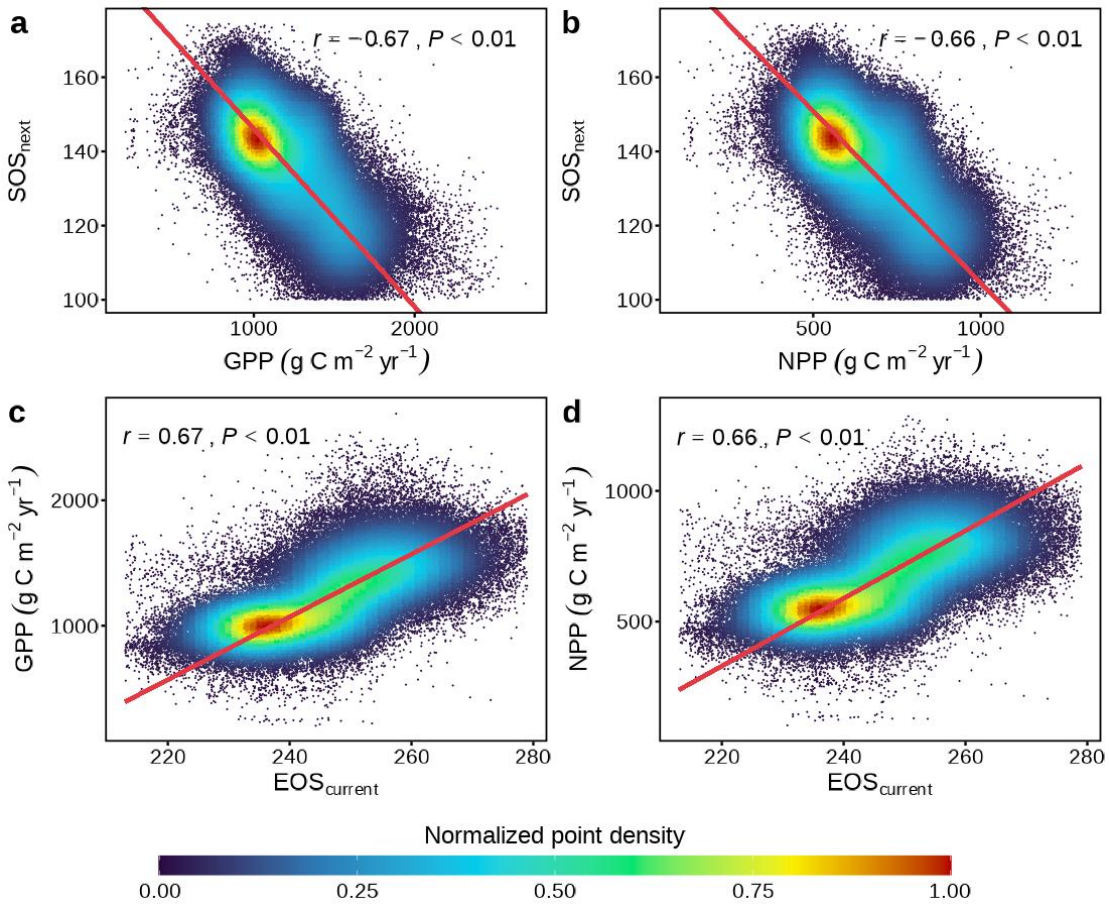


Fig. 4 The relationships between vegetation photosynthetic productivity and phenology based on GOSIF-GPP phenological product. a–**b**, Relationships between annual GPP (**a**) and NPP (**b**) and the start of growing season in the next year (SOS_{next}) under post-drought rewetting. **c**–**d**, Relationships between the end of growing season in the current year ($EOS_{current}$) and annual GPP (**c**) and NPP (**d**) under post-drought rewetting. In **a**–**d**, the red lines indicate standardized major axis (SMA) regressions of relationships, with the *r* and *P* values presented.

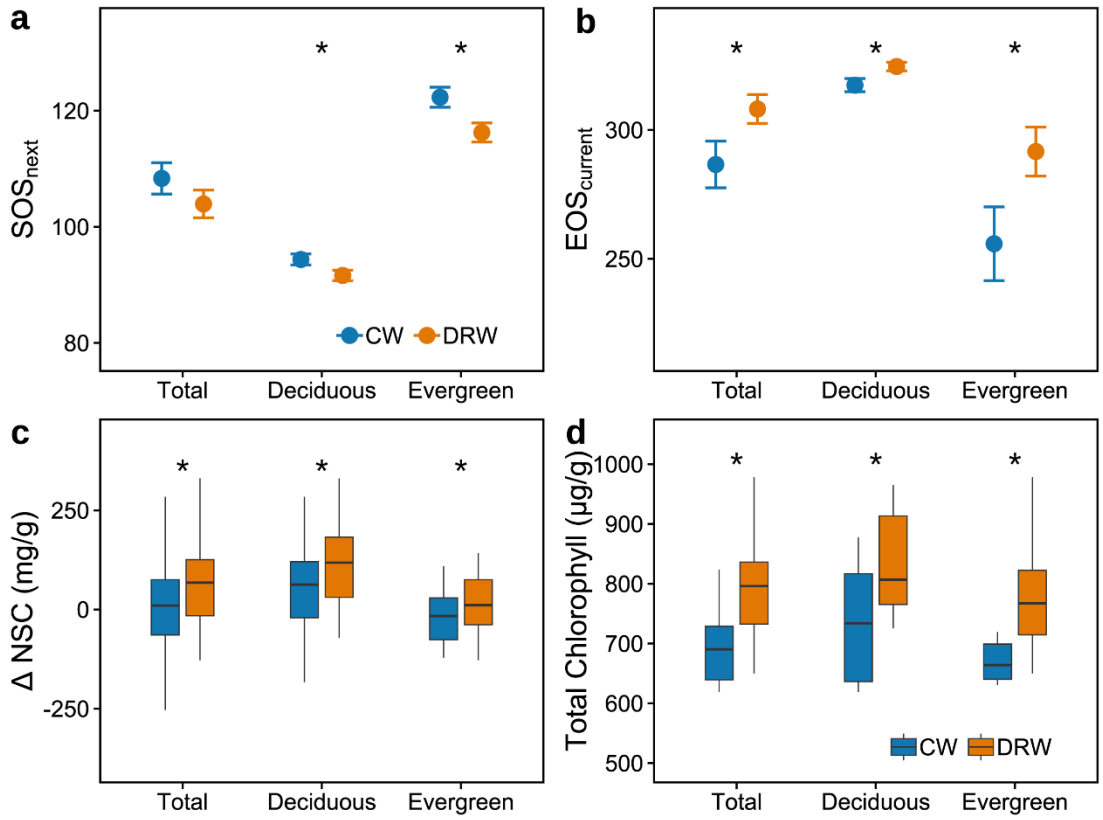
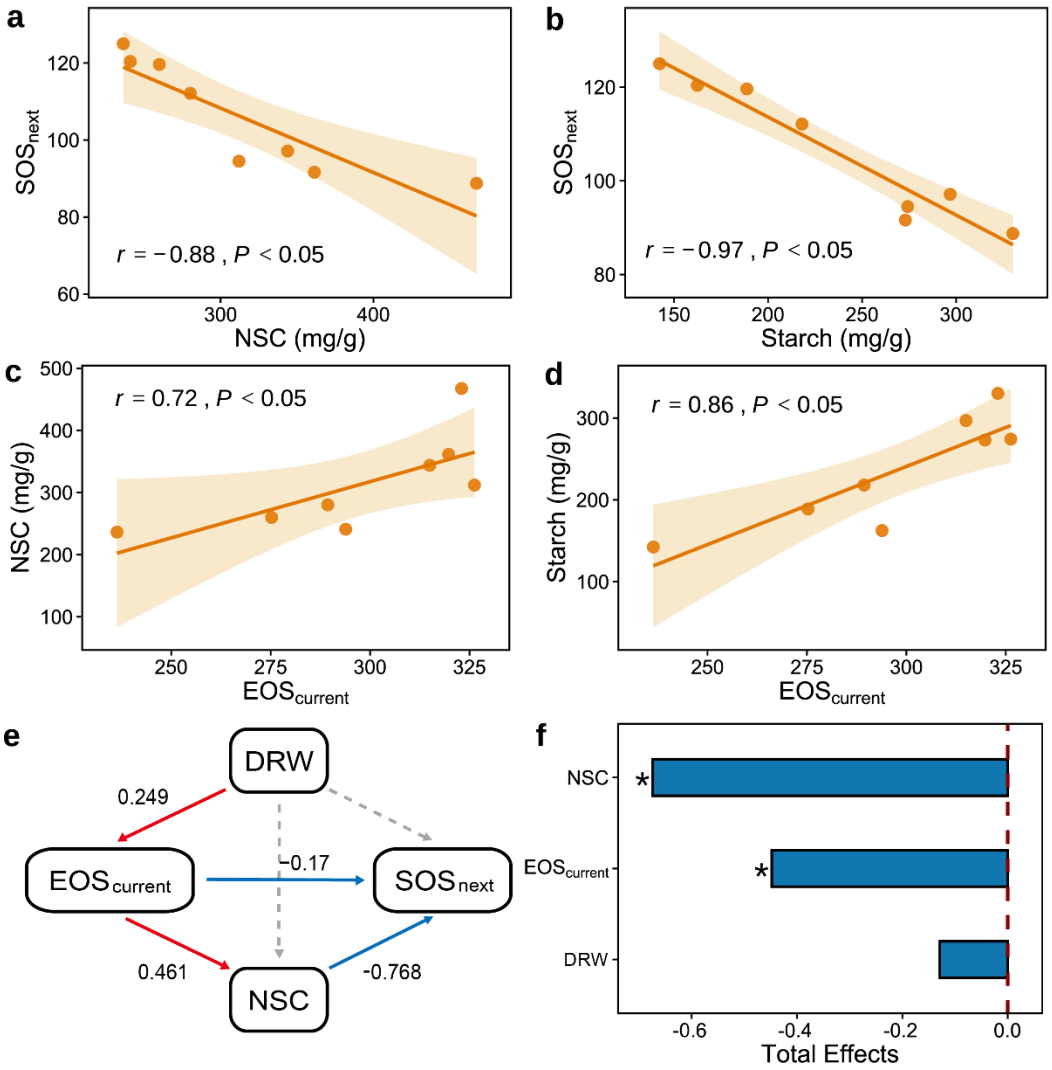


Fig. 5 Effects of experimental post-drought rewetting on phenology, non-structural carbohydrate (NSC) concentration and total chlorophyll content. a–**b**, Differences in the start of growing season in the next year (SOS_{next}) (**a**) and the end of growing season in the current year ($EOS_{current}$) (**b**) between constant-wetting (CW) and post-drought rewetting (DRW) treatments across deciduous and evergreen trees. **c**, Differences in ΔNSC between CW and DRW. ΔNSC indicates the change of NSC concentration in branch tissues from drought to rewetting phases. **d**, Differences in total chlorophyll content between CW and DRW during rewetting phase. In **a**–**b**, points and error bars plots show means ± standard errors. In **c**–**d**, boxplots show medians, interquartile ranges, and 5th–95th percentiles The asterisk in **a**–**d** indicates a significant difference between treatments (two-tailed *t*-test, $P < 0.05$).



977

978 **Fig. 6 Relationships between phenology and non-structural carbohydrate (NSC)**
979 **components in the post-drought rewetting experiments. a**–**b**, Relationships of NSC
980 (**a**) and starch (**b**) concentrations with the start of growing season in the next year
981 (SOS_{next}) in rewetting phase. **c**–**d**, Relationships of the end of growing season in current
982 year ($EOS_{current}$) with NSC (**c**) and starch (**d**) concentrations in rewetting phase. **e**,
983 Piecewise structural equation model (SEM) including post-drought rewetting (DRW),
984 $EOS_{current}$ and NSC. **f**, Standardized total effects of DRW, $EOS_{current}$ and NSC on SOS_{next}.
985 In **a**–**d**, the solid lines indicate linear regression fits and the shading areas represent 95%
986 confidence intervals. In **e**, DRW treatment, $EOS_{current}$ and NSC were incorporated into
987 the piecewise SEM to explore the direct (arrows from each factor directly pointing to
988 the SOS_{next}) or indirect (arrows from each factor firstly directly pointing to $EOS_{current}$
989 or NSC, and final to SOS_{next}) effects of factors on SOS_{next}, with blue lines indicating a
990 negative effect and red lines indicating a positive effect. The solid and dashed lines
991 denote significant (two-sided *t*-test, $P < 0.05$) and non-significant relationships,
992 respectively. The regression coefficients and other statistics were listed in Table S10. In
993 **f**, negative values indicate advancement on SOS_{next}. Red dashed line indicates zero. The
994 asterisk indicates a statistically significant total effect using 1,000 bootstrap resamples.
995 Detailed statistics of SEM were listed in Table S11.

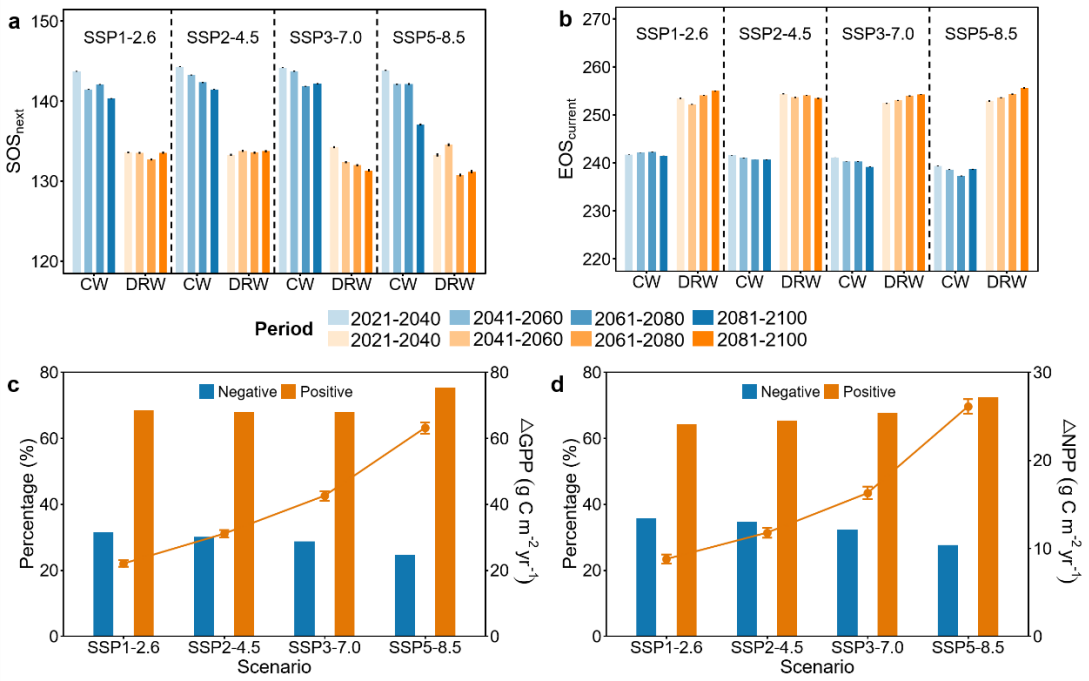
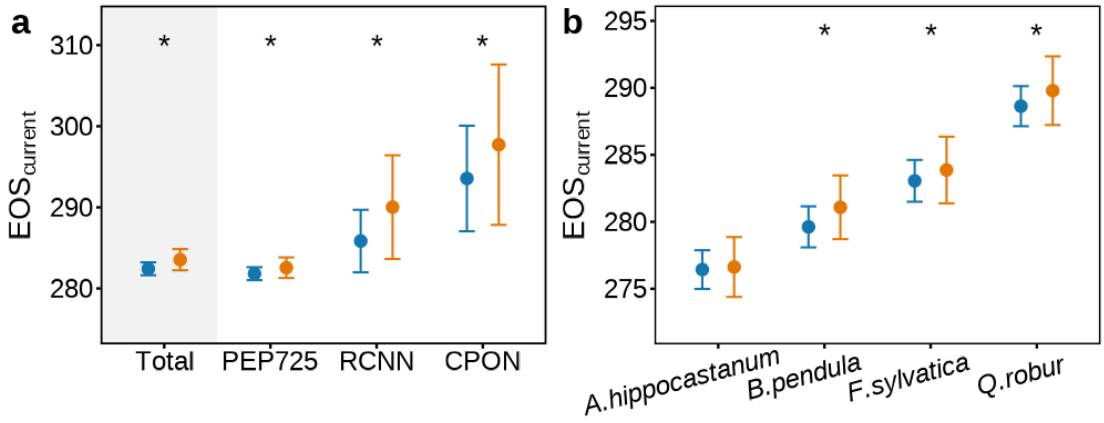


Fig. 7 Future projections of phenology and vegetation photosynthetic productivity under constant-wetting (CW) and post-drought rewetting (DRW) for four CO_2 emission scenarios. a–**b**, The start of growing season in the next year (SOS_{next}) (**a**) and the end of growing season in the current year ($EOS_{current}$) (**b**) under CW and DRW during four future periods (2021–2040, 2041–2060, 2061–2080, and 2081–2100) under four CO_2 emission scenarios (SSP1-2.6, SSP2-4.5, SSP3-7.0, and SSP5-8.5). **c**–**d**, The percentage of negative and positive values (left y-axis) and the mean value (right y-axis) of the differences in GPP (**c**) and NPP (**d**) between CW and DRW. In **a**–**b**, columns and bar plots display means ± standard errors. In **c**–**d**, the points with bars show the mean ± standard errors.

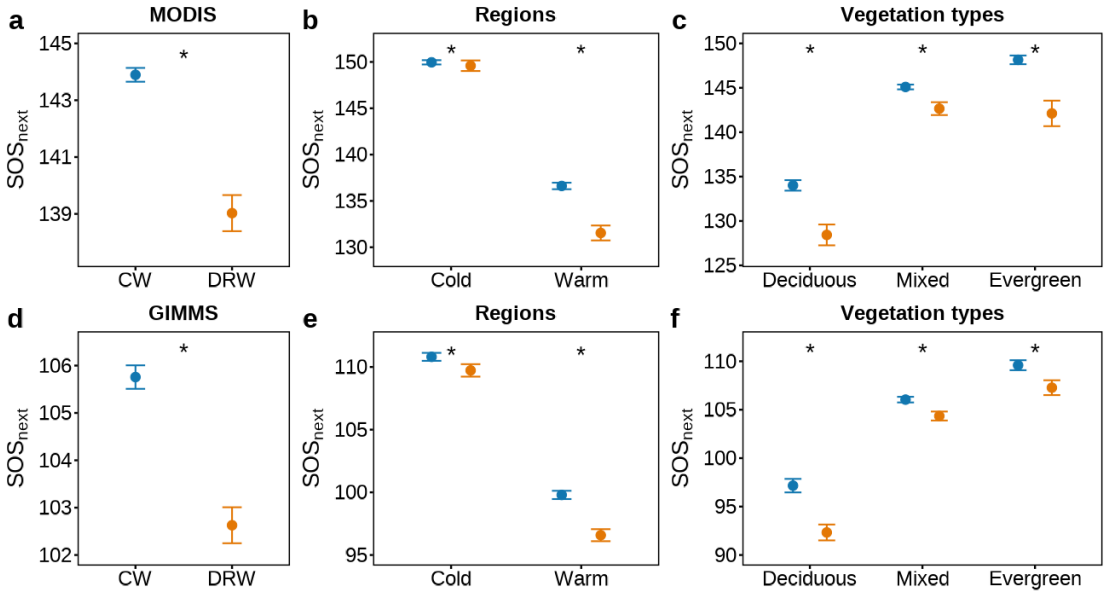
Extended data figures and tables
for
Autumn overcompensation following post-drought rewetting advances spring phenology

Minghong Yu, Yilei Jin, Jiajie Luo, Xinbo Wang, Hongshuang Gu, Haoyu Qiu, Anqi Yang, Ge Bai, Qin Yan, Junkai Ma, Josep Peñuelas, Lei Chen

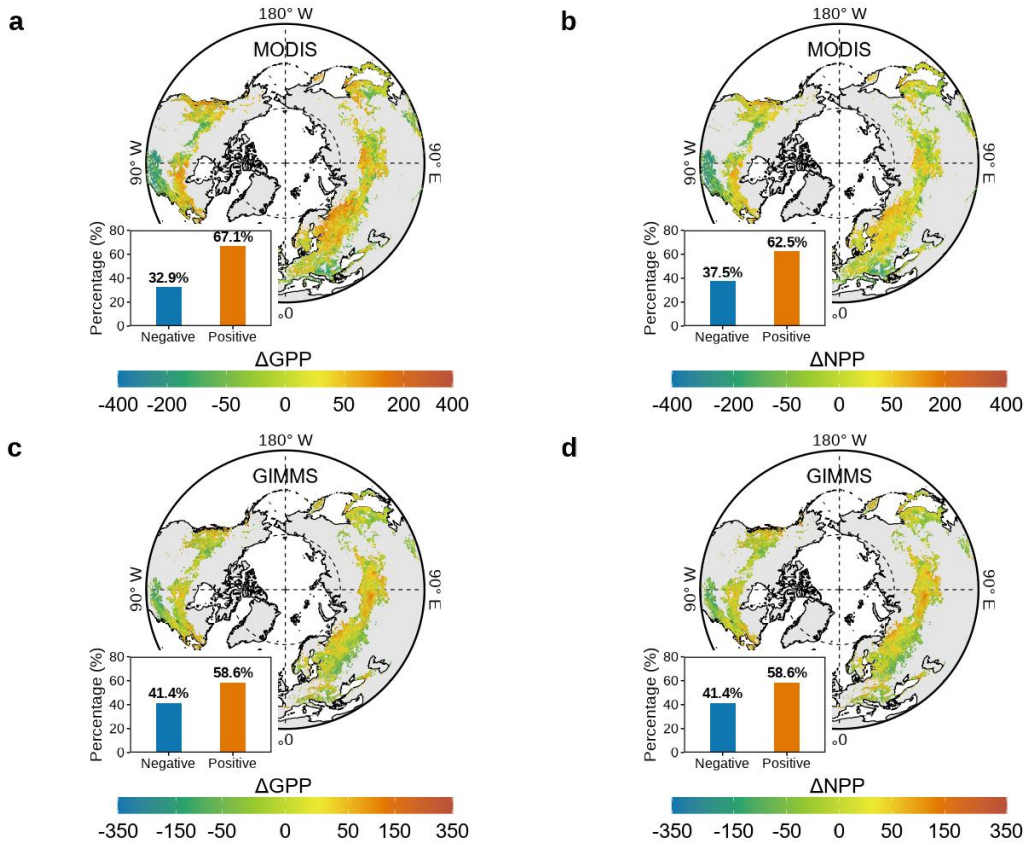
Correspondence: lei.chen1029@gmail.com



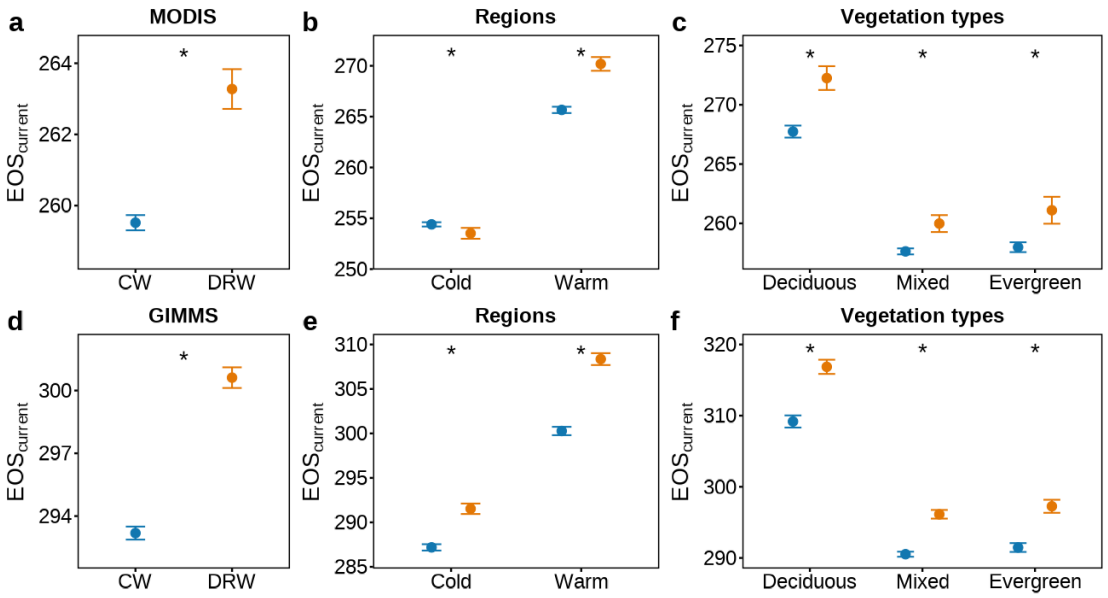
Extended Data Fig. 1 Effects of post-drought rewetting on the timing of autumn phenology across ground-based phenological networks. a, Differences in the end of growing season in the current year ($EOS_{current}$) between constant-wetting (CW) and post-drought rewetting (DRW) across three phenological datasets. **b**, Differences in $EOS_{current}$ between CW and DRW for four representative European tree species (*Aesculus hippocastanum*, *Betula pendula*, *Fagus sylvatica*, and *Quercus robur*) from the PEP725 network. Points represent mean day of year (DOY) and error bars show 10 times the 95% confidence intervals. The asterisk indicates a significant difference (two-tailed *t*-test, $P < 0.05$).



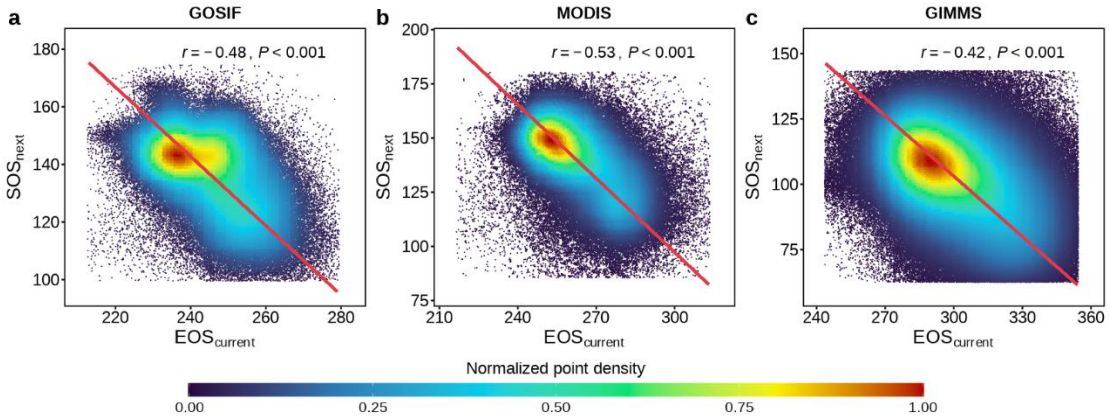
Extended Data Fig. 2 Effects of post-drought rewetting on the timing of spring phenology based on MODIS-NBAR and GIMMS NDVI3g phenological products. **a**–**c**, Differences in the start of growing season in the next year (SOS_{next}) between constant-wetting (CW) and post-drought rewetting (DRW) across the total dataset (**a**), regions (**b**), and vegetation types (**c**) based on MODIS-NBAR. **d**–**f**, Differences in SOS_{next} between CW and DRW across the total dataset (**d**), regions (**e**), and vegetation types (**f**) based on GIMMS NDVI3g. In **a**–**f**, pixels were classified into cold and warm regions based on the long-term mean temperatures, and deciduous, mixed, and evergreen based on their forest types. Points represent mean day of year (DOY) and error bars show 10 times the 95% confidence intervals. The asterisk indicates a significant difference (two-tailed *t*-test, $P < 0.05$).



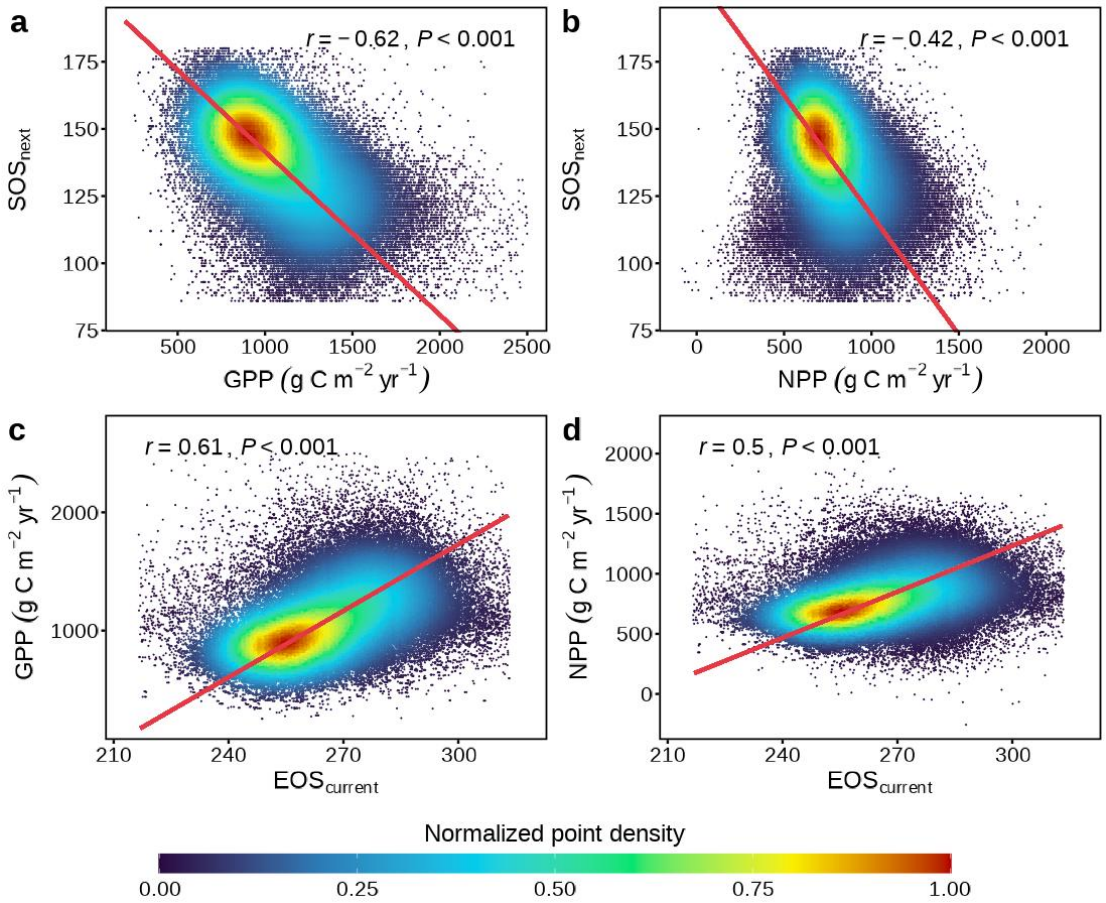
Extended Data Fig. 3 Effects of post-drought rewetting on vegetation photosynthetic productivity based on MODIS-NBAR and GIMMS NDVI3g phenological products. a–**b**, Differences in GPP (**a**) and NPP (**b**) between constant-wetting (CW) and post-drought rewetting (DRW) across the Northern Hemisphere forests based on MODIS-NBAR. **c**–**d**, Differences in GPP (**c**) and NPP (**d**) between CW and DRW across the Northern Hemisphere forests based on GIMMS NDVI3g. Insets in **a**–**d** show the percentages of negative (blue) or positive (yellow) value of difference.



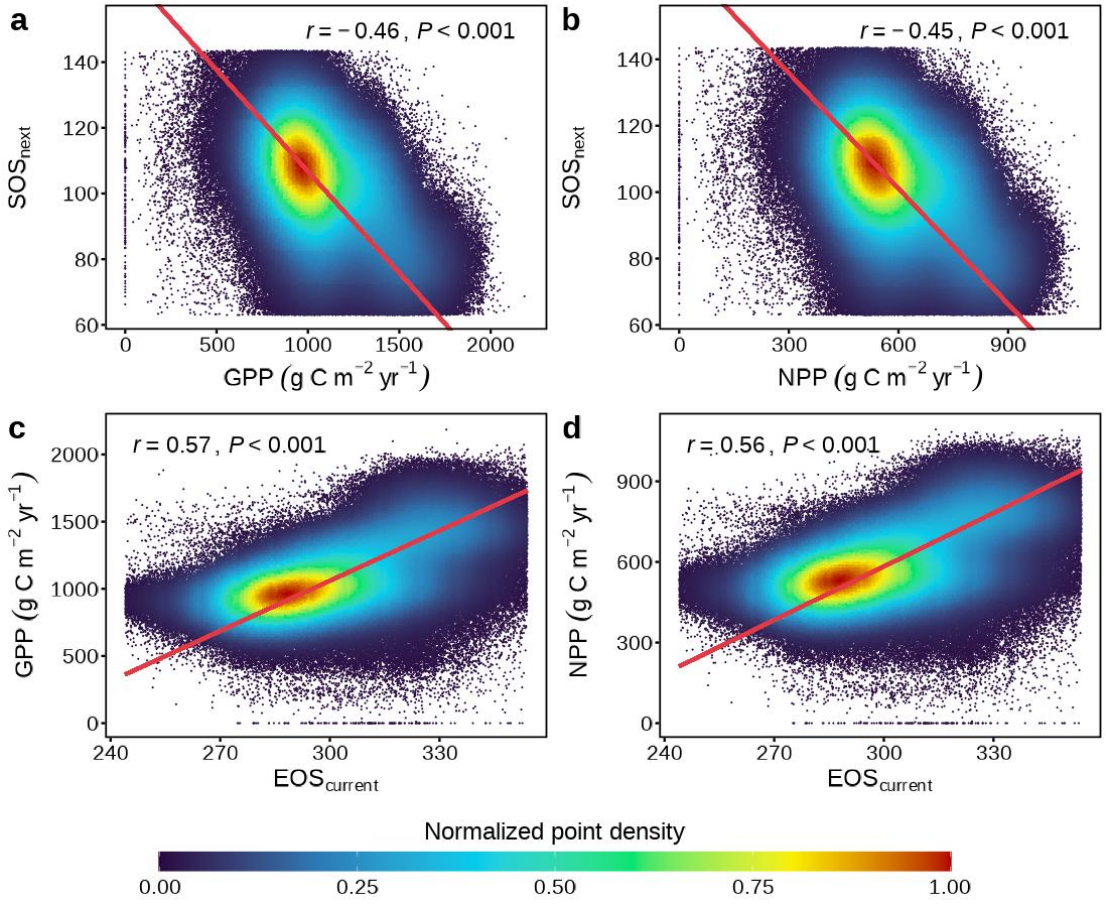
Extended Data Fig. 4 Effects of post-drought rewetting on the timing of autumn phenology based on MODIS-NBAR and GIMMS NDVI3g phenological products. **a–c**, Differences in the end of growing season in the current year ($EOS_{current}$) between constant-wetting (CW) and post-drought rewetting (DRW) across the total dataset (**a**), regions (**b**), and vegetation types (**c**) based on MODIS-NBAR. **d–f**, Differences in $EOS_{current}$ between CW and DRW across the total dataset (**d**), regions (**e**), and vegetation types (**f**) based on GIMMS NDVI3g. In **a–f**, pixels were classified into cold and warm regions based on the long-term mean temperatures, and deciduous, mixed, and evergreen based on their forest types. Points represent mean day of year (DOY) and error bars show 10 times the 95% confidence intervals. The asterisk indicates a significant difference (two-tailed *t*-test, $P < 0.05$).



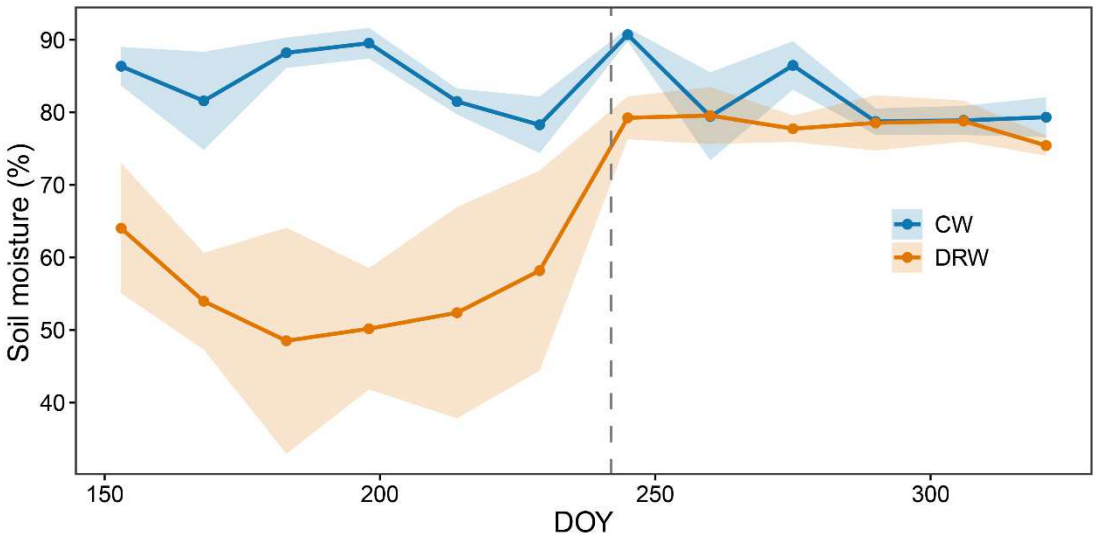
Extended Data Fig. 5 Relationships between autumn and spring phenology under post-drought rewetting based on three satellite remote-sensing datasets. a–c, Relationships between the end of growing season in the current year ($EOS_{current}$) and the start of growing season in the next year (SOS_{next}) based on GOSIF-GPP (**a**), MODIS-NBAR (**b**), and GIMMS NDVI3g (**c**) phenological products. The red lines indicate standardized major axis (SMA) regressions of relationships, with the *r* and *P* values presented.



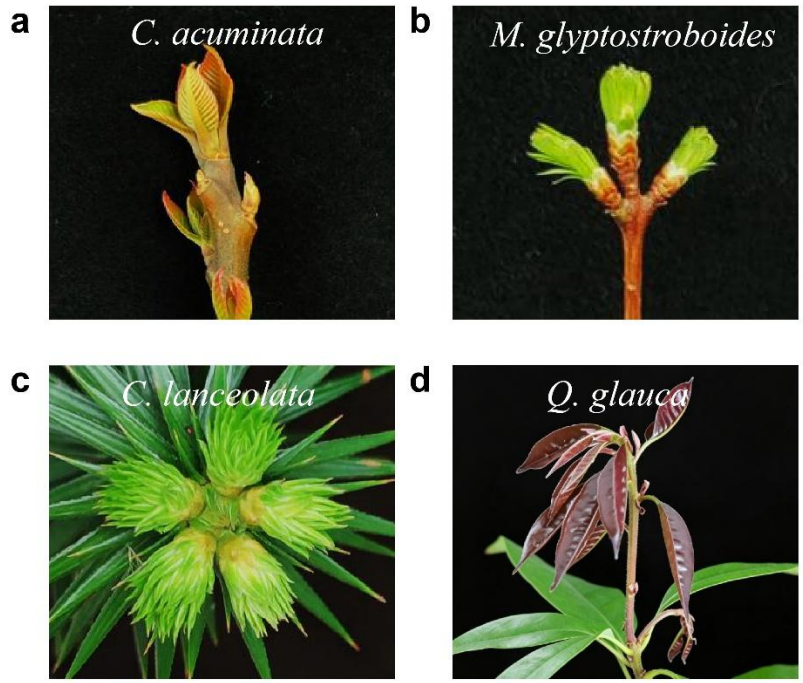
Extended Data Fig. 6 The relationships between vegetation photosynthetic productivity and phenology based on MODIS-NBAR phenological product. a–**b**, Relationships between annual GPP (**a**) and NPP (**b**) and the start of growing season in the next year (SOS_{next}) under post-drought rewetting. **c**–**d**, Relationships between the end of growing season in the current year ($EOS_{current}$) and annual GPP (**c**) and NPP (**d**) under post-drought rewetting. In **a**–**d**, the red lines indicate standardized major axis (SMA) regressions of relationships, with the *r* and *P* values presented.



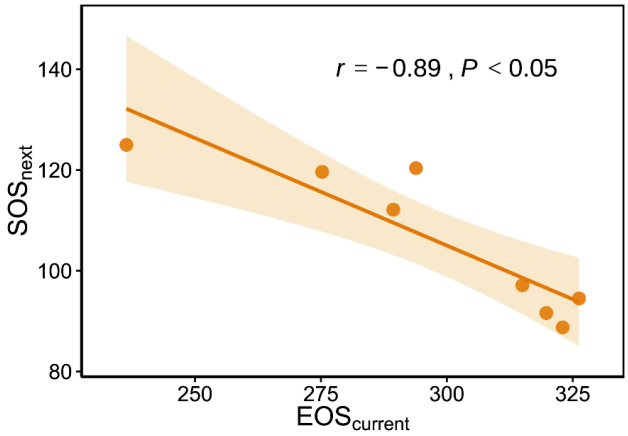
Extended Data Fig. 7 The relationships between vegetation photosynthetic productivity and phenology based on GIMMS NDVI3g phenological product. a–**b**, Relationships between annual GPP (**a**) and NPP (**b**) and the start of growing season in the next year (SOS_{next}) under post-drought rewetting. **c**–**d**, Relationships between the end of growing season in the current year ($EOS_{current}$) and annual GPP (**c**) and NPP (**d**) under post-drought rewetting. In **a**–**d**, the red lines indicate standardized major axis (SMA) regressions of relationships, with the *r* and *P* values presented.



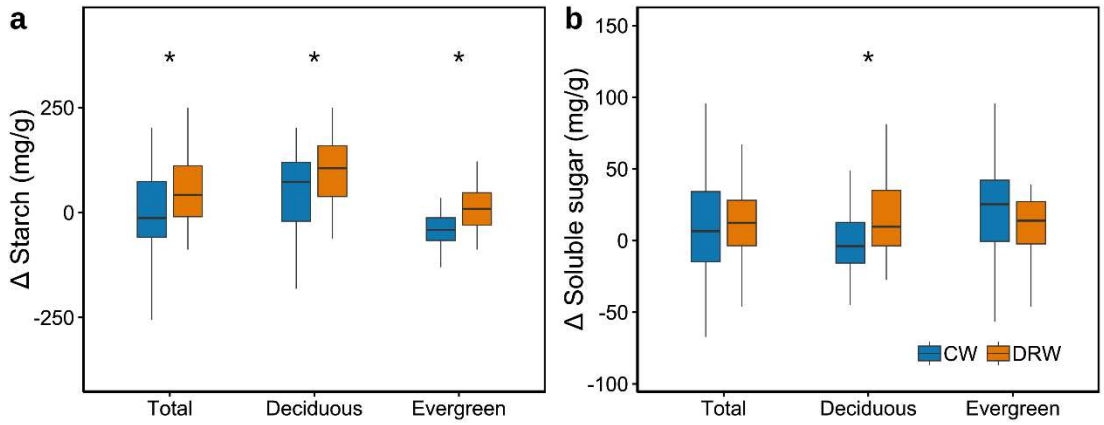
Extended Data Fig. 8 Soil moisture during drought and rewetting phases in the post-drought rewetting experiments. Points represent mean daily soil moisture for each 15-day interval. Shaded ribbon represents means ± standard deviations. The gray dashed line denotes the onset of rewetting. Treatment abbreviations: CW = constant-wetting, DRW = post-drought rewetting.



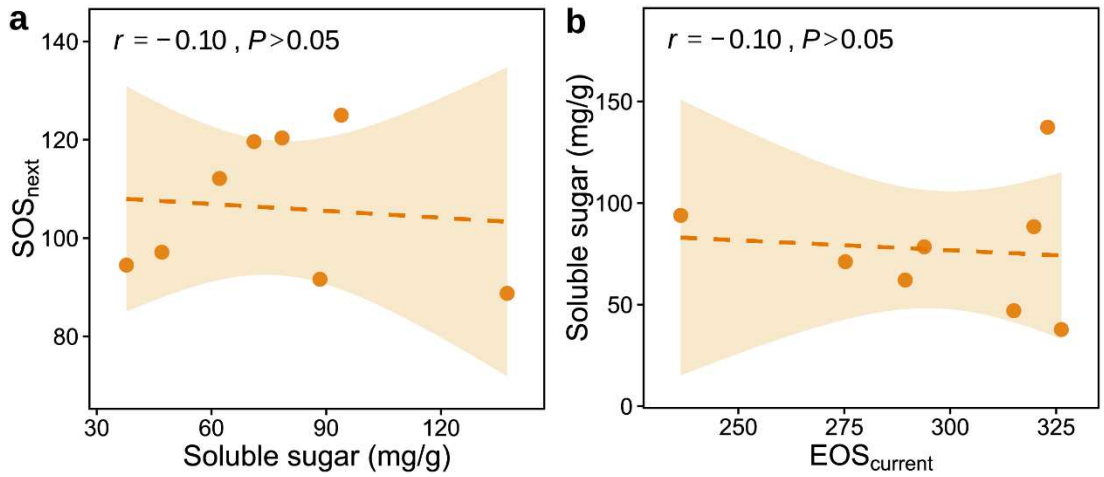
Extended Data Fig. 9 Four tree species used in the post-drought rewetting experiments. a, broadleaved deciduous, *Camptotheca acuminata* Decne. **b**, needle-leaved deciduous, *Metasequoia glyptostroboides* Hu & W.C. Cheng. **c**, needle-leaved evergreen, *Cunninghamia lanceolata* (Lamb.) Hook. **d**, broadleaved evergreen, *Quercus glauca* Thunb.



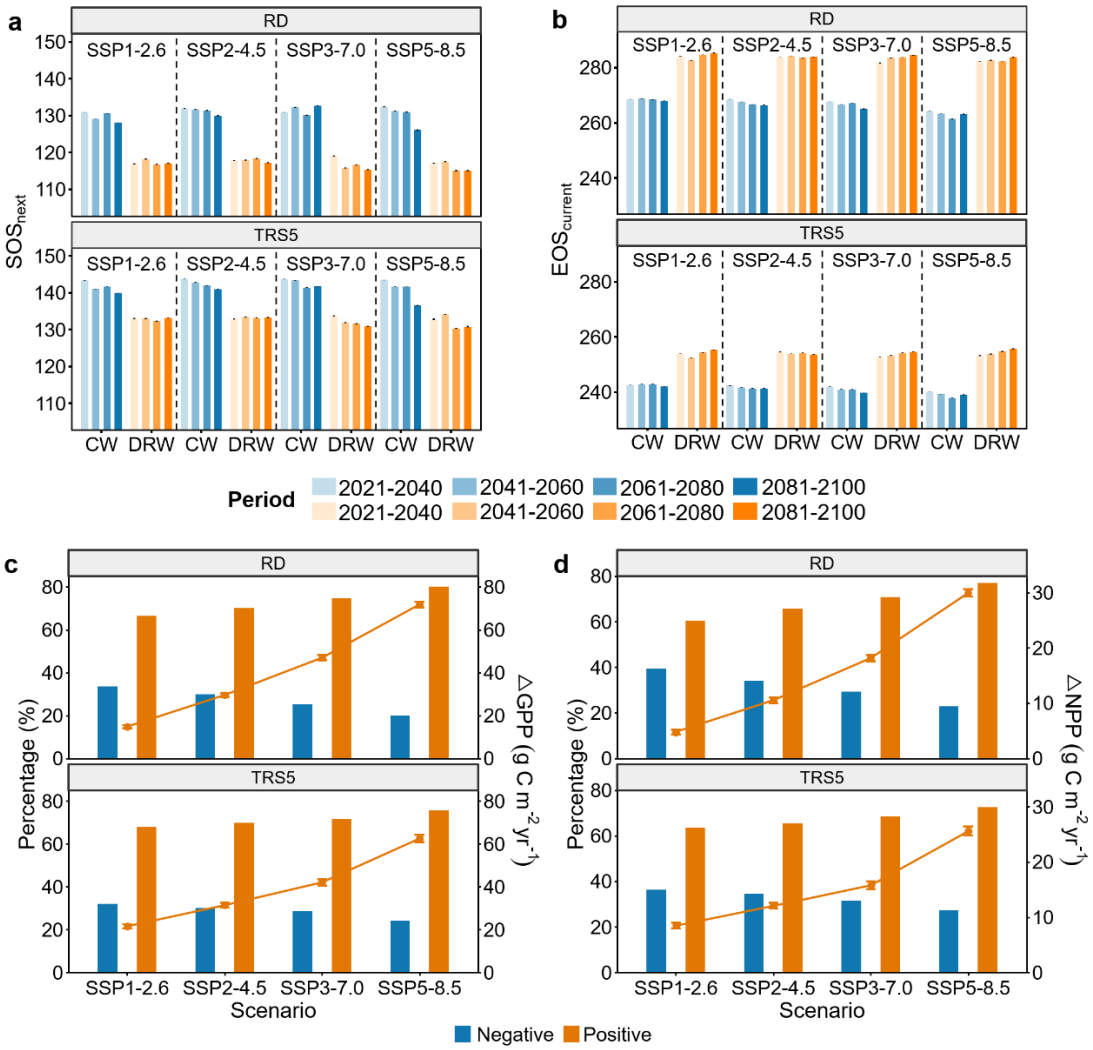
Extended Data Fig. 10 Relationship between the end of growing season in current year ($EOS_{current}$) and the start of growing season in the next year (SOS_{next}) in the post-drought rewetting experiments. The solid line denotes significant relationships (two-sided *t*-test, $P < 0.05$), with *r* indicating the correlation coefficient. The shading area represents 95% confidence intervals.



Extended Data Fig. 11 Differences in ΔStarch and ΔSoluble sugar content between constant-wetting (CW) and post-drought rewetting (DRW). a, ΔStarch indicates the change of starch concentrations in branch tissues from drought to rewetting phases. **b**, ΔSoluble sugar indicates the change of soluble sugar concentrations in branch tissues from drought to rewetting phases. In **a**–**b**, boxplots show medians, interquartile ranges, and 5th–95th percentiles. The asterisks indicate a significant difference between treatments (two-tailed *t*-test, $P < 0.05$).



Extended Data Fig. 12 Relationships between phenology and soluble sugar in the post-drought rewetting experiments. a, Relationship of soluble sugar concentration with the start of growing season in the next year (SOS_{next}) in rewetting phase. **b**, Relationship of the end of growing season in current year ($EOS_{current}$) with soluble sugar concentration in rewetting phase. In **a**–**b**, the dashed lines denote non-significant relationship using linear regression fit, with *r* indicating the correlation coefficient. The shading areas represent 95% confidence intervals.



Extended Data Fig. 13 Future projections of phenology and vegetation photosynthetic productivity under constant-wetting (CW) and post-drought rewetting (DRW) for four CO_2 emission scenarios. a–**b**, The start of growing season in the next year (SOS_{next}) (**a**) and the end of growing season in the current year ($EOS_{current}$) (**b**) under CW and DRW during four future periods (2021–2040, 2041–2060, 2061–2080, and 2081–2100) under four CO_2 emission scenarios (SSP1-2.6, SSP2-4.5, SSP3-7.0, and SSP5-8.5). **c**–**d**, The percentage of negative and positive values (left y-axis) and the mean value (right y-axis) of the differences in GPP (**c**) and NPP (**d**) between CW and DRW. In **a**–**b**, columns and bar plots display means ± standard errors. In **c**–**d**, the points with bars show the mean ± standard errors.

Supplementary Table 1 Detailed information of phenological datasets used in this study.

Dataset	Time Series	Identifier
PEP725	1982–2020	http://www.pep725.eu
RCNN	1981–2016	https://doi.org/10.1038/s41597-020-0376-z
CPON	1982–2017	http://www.cpon.ac.cn
GOSIF-GPP	2001–2020	ttps://doi.org/10.6084/m9.figshare.17195009.v3
MODIS-NBAR	2001–2020	https://doi.org/10.5067/MODIS/MCD12Q2.061
GIMMS NDVI3g	1982–2014	http://data.globalecology.unh.edu/data/GIMMS_NDVI3g_Phenology/
Future Phenology	2021–2100	https://www.geodata.cn/

Supplementary Table 2 Number of records after data filtering for each ground-based network.

Dataset	Site	Species	Simple size
PEP725	2765	14	131957
RCNN	137	180	7232
CPON	37	341	5235
Total	2939	535	144424

Supplementary Table 3 Timing of autumn and spring phenology from ground-based network datasets in this study. Timing of the start of growing season in the next year (SOS_{next}) and the end of growing season in the current year ($EOS_{current}$) under constant-wetting (CW) and post-drought rewetting (DRW) treatments. SOS_{next} and $EOS_{current}$ expressed in days of the year (means ± standard errors).

Datasets	Treatment	SOS_{next}	$EOS_{current}$
Total	CW	113.97 ± 0.04	282.43 ± 0.04
	DRW	111.18 ± 0.06	283.55 ± 0.07
PEP725	CW	113.58 ± 0.03	281.82 ± 0.04
	DRW	110.88 ± 0.06	282.56 ± 0.06
RCNN	CW	123.53 ± 0.22	285.84 ± 0.20
	DRW	122.17 ± 0.40	290.03 ± 0.33
CPON	CW	109.95 ± 0.30	293.56 ± 0.33
	DRW	105.16 ± 0.41	297.73 ± 0.50
A. hippocastanum	CW	109.28 ± 0.06	276.43 ± 0.07
	DRW	106.30 ± 0.10	276.63 ± 0.11
B. pendula	CW	108.80 ± 0.06	279.62 ± 0.08
	DRW	105.85 ± 0.09	281.08 ± 0.12
F. sylvatica	CW	116.02 ± 0.06	283.06 ± 0.08
	DRW	114.08 ± 0.09	283.87 ± 0.13
Q.robur	CW	121.00 ± 0.06	288.63 ± 0.08
	DRW	118.76 ± 0.10	289.79 ± 0.13

Supplementary Table 4 Timing of spring and autumn phenology from three satellite-derived phenology datasets in this study. Timing of the start of growing season in the next year (SOS_{next}) and the end of growing season in the current year ($EOS_{current}$) under constant-wetting (CW) and post-drought rewetting (DRW) treatments of different groups. SOS_{next} and $EOS_{current}$ expressed in days of the year (means ± standard errors).

Dataset	Group	Treatment	SOS_{next}	$EOS_{current}$
GOSIF	Total	CW	140.76 ± 0.01	242.72 ± 0.01
		DRW	136.23 ± 0.03	245.43 ± 0.03
	Cold	CW	146.50 ± 0.01	238.91 ± 0.01
		DRW	145.90 ± 0.03	238.39 ± 0.03
	Warm	CW	133.74 ± 0.02	247.38 ± 0.02
		DRW	128.72 ± 0.04	250.90 ± 0.03
	Deciduous	CW	132.32 ± 0.03	251.86 ± 0.03
		DRW	127.00 ± 0.07	254.30 ± 0.05
	Mixed	CW	142.08 ± 0.01	240.79 ± 0.01
		DRW	139.48 ± 0.04	242.53 ± 0.03
	Evergreen	CW	142.69 ± 0.03	242.02 ± 0.02
		DRW	137.61 ± 0.08	243.52 ± 0.06
MODIS	Total	CW	143.89 ± 0.01	259.52 ± 0.01
		DRW	139.03 ± 0.03	263.28 ± 0.03
	Cold	CW	149.96 ± 0.01	254.40 ± 0.01
		DRW	149.59 ± 0.03	253.52 ± 0.03
	Warm	CW	136.61 ± 0.02	265.66 ± 0.02
		DRW	131.54 ± 0.04	270.19 ± 0.03
	Deciduous	CW	134.01 ± 0.03	267.74 ± 0.03
		DRW	128.43 ± 0.06	272.25 ± 0.05
	Mixed	CW	145.09 ± 0.01	257.64 ± 0.01
		DRW	142.65 ± 0.04	259.98 ± 0.04
	Evergreen	CW	148.15 ± 0.03	257.99 ± 0.01
		DRW	142.12 ± 0.07	261.11 ± 0.06
GIMMS	Total	CW	101.04 ± 0.01	299.85 ± 0.02
		DRW	96.96 ± 0.02	306.38 ± 0.02
	Cold	CW	110.81 ± 0.02	287.19 ± 0.02
		DRW	109.73 ± 0.03	291.53 ± 0.03
	Warm	CW	99.79 ± 0.02	300.27 ± 0.02
		DRW	96.58 ± 0.02	308.36 ± 0.03
	Deciduous	CW	93.65 ± 0.04	315.07 ± 0.04
		DRW	88.96 ± 0.04	321.67 ± 0.05
	Mixed	CW	101.58 ± 0.02	297.14 ± 0.02
		DRW	98.52 ± 0.03	302.20 ± 0.03
	Evergreen	CW	104.21 ± 0.03	297.03 ± 0.03
		DRW	100.21 ± 0.05	302.79 ± 0.05

Supplementary Table 5 Linear mixed-effects model results for post-drought rewetting effects on spring and autumn phenology across different regions and vegetation types using GOSIF-GPP phenological product. Models were fitted separately for the start of growing season in the next year (SOS_{next}) and the end of growing season in the current year ($EOS_{current}$). Within each model, the timing of phenology was the response variable. Treatments (constant-wetting, CW and post-drought rewetting, DRW) and its interaction with regions or vegetation types were the fixed effects, with site included as random intercept. Pixels were divided into cold and warm regions and deciduous, mixed, and evergreen frosts. CW, deciduous, and cold region were set as the reference levels.

Phenology	Group	Variables	Estimate	*SE*	*t* value	*P* value
SOS_{next}	Regions	Intercept	146.50	0.04	3782.70	< 0.01
		DRW	−0.42	0.02	−16.92	< 0.01
		Warm	−14.99	0.06	−272.18	< 0.01
		DRW×Warm	−0.43	0.03	−12.79	< 0.01
	Vegetation types	Intercept	130.00	0.08	1609.71	< 0.01
		DRW	−0.93	0.04	−24.66	< 0.01
		Evergreen	11.32	0.11	104.16	< 0.01
		Mixed	10.97	0.09	118.02	< 0.01
		DRW×Evergreen	0.00	0.05	0.01	0.99
		DRW×Mixed	0.57	0.04	12.87	< 0.01
$EOS_{current}$	Regions	Intercept	239.30	0.04	6155.01	< 0.01
		DRW	−1.74	0.02	−93.01	< 0.01
		Warm	9.32	0.06	168.96	< 0.01
		DRW×Warm	2.16	0.03	83.53	< 0.01
	Vegetation types	Intercept	252.20	0.07	3768.69	< 0.01
		DRW	0.73	0.03	25.15	< 0.01
		Evergreen	−9.01	0.09	−99.94	< 0.01
		Mixed	−10.55	0.08	−136.97	< 0.01
		DRW×Evergreen	−2.42	0.04	−60.66	< 0.01
		DRW×Mixed	−1.39	0.03	−41.44	< 0.01

Supplementary Table 6 Linear mixed-effects model results for post-drought rewetting effects on spring and autumn phenology across different regions and vegetation types using MODIS-NBAR phenological product. Models were fitted separately for the start of growing season in the next year (SOS_{next}) and the end of growing season in the current year ($EOS_{current}$). Within each model, the timing of phenology was the response variable. Treatments (constant-wetting, CW and post-drought rewetting, DRW) and its interaction with regions or vegetation types were the fixed effects, with pixel included as random intercept. Pixels were divided into cold and warm regions and deciduous, mixed, and evergreen frosts. CW, deciduous, and cold region were set as the reference levels.

Phenology	Group	Variables	Estimate	*SE*	*t* value	*P* value
SOS_{next}	Regions	Intercept	150.10	0.04	3629.82	< 0.01
		DRW	−0.18	0.03	−7.04	< 0.01
		Warm	−15.71	0.06	−267.56	< 0.01
		DRW×Warm	−0.59	0.04	−17.13	< 0.01
	Vegetation types	Intercept	132.60	0.08	1696.38	< 0.01
		DRW	−1.30	0.04	−35.64	< 0.01
		Evergreen	13.59	0.10	131.03	< 0.01
		Mixed	11.23	0.09	122.03	< 0.01
		DRW×Evergreen	0.03	0.05	0.62	0.54
		DRW×Mixed	1.50	0.04	34.57	< 0.01
$EOS_{current}$	Regions	Intercept	254.60	0.03	7708.76	< 0.01
		DRW	−1.25	0.02	−51.26	< 0.01
		Warm	1.20	0.05	255.00	< 0.01
		DRW×Warm	3.46	0.03	104.67	< 0.01
	Vegetation types	Intercept	267.80	0.06	4203.14	< 0.01
		DRW	2.19	0.04	62.57	< 0.01
		Evergreen	−8.76	0.08	−103.67	< 0.01
		Mixed	−9.13	0.07	−121.85	< 0.01
		DRW×Evergreen	−1.79	0.05	−37.10	< 0.01
		DRW×Mixed	−2.09	0.04	−49.96	< 0.01

Supplementary Table 7 Linear mixed-effects model results for post-drought rewetting effects on spring and autumn phenology across different regions and vegetation types using GIMMS NDVI3g phenological product. Models were fitted separately for the start of growing season in the next year (SOS_{next})and the end of growing season in the current year ($EOS_{current}$). Within each model, the timing of phenology was the response variable. Treatments (constant-wetting, CW and post-drought rewetting, DRW) and its interaction with regions or vegetation types were the fixed effects, with site included as random intercept. Pixels were divided into cold and warm regions and deciduous, mixed, and evergreen frosts. CW, deciduous, and cold region were set as the reference levels.

Phenology	Group	Variables	Estimate	*SE*	*t* value	*P* value
SOS_{next}	Regions	Intercept	110.50	0.04	2716.64	< 0.01
		DRW	−0.35	0.02	−14.53	< 0.01
		Warm	−12.41	0.06	−214.57	< 0.01
		DRW×Warm	−1.01	0.03	−29.50	< 0.01
	Vegetation types	Intercept	96.07	0.07	1362.74	< 0.01
		DRW	−0.88	0.04	−20.92	< 0.01
		Evergreen	13.18	0.09	150.65	< 0.01
		Mixed	8.63	0.08	111.38	< 0.01
		DRW×Evergreen	−0.26	0.05	−4.71	< 0.01
		DRW×Mixed	0.15	0.05	3.14	< 0.01
$EOS_{current}$	Regions	Intercept	288.90	0.06	4511.63	< 0.01
		DRW	2.11	0.03	84.18	< 0.01
		Warm	15.95	0.09	175.65	< 0.01
		DRW×Warm	−0.19	0.04	−5.41	< 0.01
	Vegetation types	Intercept	307.10	0.10	3212.43	< 0.01
		DRW	2.55	0.04	59.05	< 0.01
		Evergreen	−15.78	0.12	−137.42	< 0.01
		Mixed	−11.08	0.10	−108.66	< 0.01
		DRW×Evergreen	−0.15	0.06	−2.60	< 0.01
		DRW×Mixed	−0.88	0.05	−17.86	< 0.01

Supplementary Table 8 Timing of spring and autumn phenology under four warming scenarios in the future based on four CMIP6 models. Timing of the start of growing season in the next year (SOS_{next}) and the end of growing season in the current year ($EOS_{current}$) under constant-wetting (CW) and post-drought rewetting (DRW) during four future periods (2021–2040, 2041–2060, 2061–2080, and 2081–2100) under four warming scenarios (SSP1-2.6, SSP2-4.5, SSP3-7.0, and SSP5-8.5) based on three phenological extraction methods. SOS_{next} and $EOS_{current}$ were mean value of four CMIP6 models, expressed in days of the year (means ± standard errors). (**a**) the derivative phenological extraction method (DER)

Scenario	Period	Treatment	SOS_{next}	$EOS_{current}$
SSP1-2.6	2021–2040	CW	143.76 ± 0.06	241.77 ± 0.05
		DRW	133.61 ± 0.14	253.48 ± 0.12
	2041–2060	CW	141.47 ± 0.06	242.19 ± 0.06
		DRW	133.55 ± 0.12	252.21 ± 0.10
	2061–2080	CW	142.08 ± 0.06	242.32 ± 0.06
		DRW	132.73 ± 0.12	254.11 ± 0.10
	2081–2100	CW	140.32 ± 0.07	241.49 ± 0.07
		DRW	133.57 ± 0.12	255.00 ± 0.11
SSP2-4.5	2021–2040	CW	144.32 ± 0.06	241.60 ± 0.05
		DRW	133.27 ± 0.15	254.42 ± 0.13
	2041–2060	CW	143.30 ± 0.06	241.06 ± 0.06
		DRW	133.80 ± 0.14	253.69 ± 0.12
	2061–2080	CW	142.36 ± 0.06	240.74 ± 0.07
		DRW	133.58 ± 0.13	254.09 ± 0.12
	2081–2100	CW	141.47 ± 0.07	240.72 ± 0.08
		DRW	133.76 ± 0.13	253.50 ± 0.11
SSP3-7.0	2021–2040	CW	144.18 ± 0.06	241.12 ± 0.06
		DRW	134.26 ± 0.13	252.47 ± 0.12
	2041–2060	CW	143.76 ± 0.07	240.30 ± 0.06
		DRW	132.39 ± 0.15	253.03 ± 0.13
	2061–2080	CW	141.87 ± 0.07	240.33 ± 0.07
		DRW	132.00 ± 0.14	253.96 ± 0.12
	2081–2100	CW	142.20 ± 0.08	239.20 ± 0.09
		DRW	131.36 ± 0.15	254.29 ± 0.13
SSP5-8.5	2021–2040	CW	143.86 ± 0.08	239.39 ± 0.08
		DRW	133.29 ± 0.17	252.92 ± 0.15
	2041–2060	CW	142.13 ± 0.08	238.65 ± 0.09
		DRW	134.56 ± 0.17	253.59 ± 0.15
	2061–2080	CW	142.17 ± 0.11	237.29 ± 0.11
		DRW	130.78 ± 0.18	254.34 ± 0.16
	2081–2100	CW	137.07 ± 0.13	238.68 ± 0.15
		DRW	131.19 ± 0.19	255.61 ± 0.17

(**b**) the Gu phenological extraction method (RD)

Scenario	Period	Treatment	SOS_{next}	$EOS_{current}$
SSP1-2.6	2021–2040	CW	130.90 ± 0.08	268.47 ± 0.08
		DRW	116.86 ± 0.14	284.01 ± 0.11
	2041–2060	CW	129.04 ± 0.09	268.79 ± 0.09
		DRW	118.17 ± 0.13	282.57 ± 0.09
	2061–2080	CW	130.60 ± 0.09	268.40 ± 0.09
		DRW	116.72 ± 0.13	284.57 ± 0.09
	2081–2100	CW	128.07 ± 0.10	267.93 ± 0.09
		DRW	117.04 ± 0.14	285.28 ± 0.10
SSP2-4.5	2021–2040	CW	131.94 ± 0.08	268.52 ± 0.08
		DRW	117.75 ± 0.15	283.59 ± 0.11
	2041–2060	CW	131.68 ± 0.09	267.53 ± 0.09
		DRW	117.92 ± 0.14	284.16 ± 0.11
	2061–2080	CW	131.39 ± 0.09	266.66 ± 0.10
		DRW	118.25 ± 0.14	283.50 ± 0.11
	2081–2100	CW	129.93 ± 0.11	266.40 ± 0.11
		DRW	117.23 ± 0.14	283.93 ± 0.10
SSP3-7.0	2021–2040	CW	130.91 ± 0.09	267.65 ± 0.08
		DRW	118.96 ± 0.14	281.68 ± 0.11
	2041–2060	CW	132.20 ± 0.10	266.59 ± 0.09
		DRW	115.77 ± 0.15	283.55 ± 0.11
	2061–2080	CW	130.11 ± 0.11	267.19 ± 0.10
		DRW	116.59 ± 0.14	283.68 ± 0.10
	2081–2100	CW	132.68 ± 0.12	265.03 ± 0.12
		DRW	115.35 ± 0.15	284.46 ± 0.11
SSP5-8.5	2021–2040	CW	132.39 ± 0.11	264.29 ± 0.10
		DRW	117.02 ± 0.17	282.16 ± 0.13
	2041–2060	CW	131.26 ± 0.12	263.25 ± 0.12
		DRW	117.44 ± 0.18	282.63 ± 0.13
	2061–2080	CW	130.95 ± 0.16	261.39 ± 0.15
		DRW	114.98 ± 0.17	282.34 ± 0.14
	2081–2100	CW	126.06 ± 0.20	263.14 ± 0.21
		DRW	115.01 ± 0.19	283.80 ± 0.14

(**c**) the 50% threshold phenological extraction method (TRS5)

Scenario	Period	Treatment	SOS_{next}	$EOS_{current}$
SSP1-2.6	2021–2040	CW	143.33 ± 0.06	242.51 ± 0.05
		DRW	133.04 ± 0.14	253.86 ± 0.12
	2041–2060	CW	141.08 ± 0.07	242.86 ± 0.06
		DRW	133.05 ± 0.12	252.41 ± 0.10
	2061–2080	CW	141.72 ± 0.06	242.86 ± 0.06
		DRW	132.33 ± 0.12	254.32 ± 0.10
	2081–2100	CW	139.94 ± 0.07	242.06 ± 0.07
		DRW	133.24 ± 0.12	255.25 ± 0.11
SSP2-4.5	2021–2040	CW	143.88 ± 0.06	242.40 ± 0.05
		DRW	132.94 ± 0.15	254.58 ± 0.12
	2041–2060	CW	142.89 ± 0.06	241.76 ± 0.06
		DRW	133.42 ± 0.14	253.88 ± 0.12
	2061–2080	CW	141.95 ± 0.06	241.36 ± 0.07
		DRW	133.16 ± 0.13	254.23 ± 0.12
	2081–2100	CW	141.05 ± 0.08	241.39 ± 0.07
		DRW	133.27 ± 0.13	253.67 ± 0.11
SSP3-7.0	2021–2040	CW	143.72 ± 0.06	241.96 ± 0.05
		DRW	133.78 ± 0.13	252.71 ± 0.12
	2041–2060	CW	143.37 ± 0.07	241.02 ± 0.06
		DRW	131.91 ± 0.15	253.29 ± 0.12
	2061–2080	CW	141.46 ± 0.07	240.99 ± 0.07
		DRW	131.58 ± 0.14	254.26 ± 0.12
	2081–2100	CW	141.81 ± 0.09	239.72 ± 0.08
		DRW	130.94 ± 0.15	254.64 ± 0.13
SSP5-8.5	2021–2040	CW	143.48 ± 0.08	240.22 ± 0.07
		DRW	132.79 ± 0.17	253.22 ± 0.15
	2041–2060	CW	141.72 ± 0.09	239.37 ± 0.09
		DRW	134.17 ± 0.17	253.84 ± 0.14
	2061–2080	CW	141.63 ± 0.11	237.99 ± 0.11
		DRW	130.34 ± 0.17	254.75 ± 0.15
	2081–2100	CW	136.55 ± 0.13	239.06 ± 0.15
		DRW	130.80 ± 0.19	255.77 ± 0.17

Supplementary Table 9 Soil temperature and soil moisture under constant-wetting (CW) and post-drought rewetting (DRW) treatments during drought and rewetting period in the experiments.

Treatment	Period	T_{mean} (℃)	Soil moisture (%)
CW	drought	26.67	84.24
	rewetting	19.93	82.26
DRW	drought	27.19	54.54
	rewetting	19.65	78.22

Supplementary Table 10 Statistical results of the piecewise structural equation model (SEM) using experimental data. The direct and indirect effects of post-drought rewetting (DRW) treatment, the end of growing season in current year ($EOS_{current}$), and non-structural carbohydrate (NSC) concentrations on the start of growing season in the next year (SOS_{next}) were incorporated into the SEM. DRW, $EOS_{current}$, and NSC were assumed to have a direct influence on SOS_{next}. DRW and $EOS_{current}$ were assumed to influence SOS_{next} indirectly by altering NSC. The standardized estimates represent the direct effect of the predictors on the responses.

Response	Predictor	Estimate	*P* Value
$EOS_{current}$	DRW	0.25	<0.05
NSC	DRW	0.06	0.63
NSC	$EOS_{current}$	0.46	<0.05
SOS_{next}	DRW	0.02	0.77
SOS_{next}	$EOS_{current}$	−0.17	<0.05
SOS_{next}	NSC	−0.77	<0.05

Supplementary Table 11 Effect decomposition of the structural equation model (SEM). Standardized direct, indirect, and total effects of post-drought rewetting (DRW) treatment, the end of growing season in current year ($EOS_{current}$), and non-structural carbohydrate (NSC) on the start of growing season in the next year (SOS_{next}) were estimated using SEM. Bootstrap resampling with 1,000 iterations was used to estimate robust 95% confidence intervals. Direct effects quantify immediate pathways; indirect effects represent mediation via $EOS_{current}$ and NSC; total effects aggregate all pathways. Confidence intervals excluding zero indicate statistical significance (*).

Predictor	Effect type	Effect	95% CI	Significance
DRW	Direct	0.019	[−0.106, 0.136]	n.s.
	Indirect	−0.148	[−0.281, 0.025]	n.s.
	Total	−0.129	[−0.305, 0.090]	n.s.
$EOS_{current}$	Direct	−0.147	[−0.265, −0.009]	*
	Indirect	−0.301	[−0.368, −0.237]	*
	Total	−0.448	[−0.552, −0.263]	*
NSC	Direct	−0.674	[−0.794, −0.542]	*
	Total	−0.674	[−0.794, −0.542]	*